processes

MDPI

Article

Multi-Objective Optimization Design and Experimental Investigation for a Prismatic Lithium-Ion Battery Integrated with a Multi-Stage Tesla Valve-Based Cold Plate

Yiwei Fan [1,2], Zhaohui Wang [1,2,*], Xiao Xiong [1,2], Satyam Panchal [3], Roydon Fraser [3] and Michael Fowler [4]

1 Key Laboratory of Metallurgical Equipment and Control Technology of Ministry of Education, Wuhan University of Science and Technology, Wuhan 430081, China; wendell93@wust.edu.cn (Y.F.); wustxxiong@163.com (X.X.)
2 Hubei Longzhong Laboratory, Xiangyang 441000, China
3 Mechanical and Mechatronic Engineering Department, University of Waterloo, 200 University Avenue West, Waterloo, ON N2L 3G1, Canada; satyam.panchal@uwaterloo.ca (S.P.); rafraser@uwaterloo.ca (R.F.)
4 Chemical Engineering Department, University of Waterloo, 200 University Avenue West, Waterloo, ON N2L 3G1, Canada; mfowler@uwaterloo.ca
* Correspondence: wustzhwang@163.com

Abstract: High current rate charging causes inevitable severe heat generation, thermal inconsistency, and even thermal runaway of lithium-ion batteries. Concerning this, a liquid cooling plate comprising a multi-stage Tesla valve (MSTV) configuration with high recognition in microfluidic applications was proposed to provide a safer temperature range for a prismatic-type lithium-ion battery. Meanwhile, a surrogate model with the objectives of the cooling performance and energy cost was constructed, and the impact of some influential design parameters was explored through the robustness analysis of the model. On this basis, the multi-objective optimization design of the neighborhood cultivation genetic algorithm (NCGA) was carried out. The obtained results demonstrated that if the MSTV channel was four channels, the valve-to-valve distance was 14.79 mm, and the thickness was 0.94 mm, the cold plate had the most effective cooling performance and a lower pumping power consumption. Finally, the optimization results were verified by a numerical simulation and an experiment, and the performance evaluation was compared with the traditional serpentine channel. The results reported that the optimized design reduced the maximum temperature and standard surface standard deviation of the cold plate by 26% and 35%, respectively. The additional pump power consumption was 17.3%. This research guides the design of battery thermal management systems to improve efficiency and energy costs, especially under the high current rate charging conditions of lithium-ion batteries.

Keywords: high current rate; multi-stage Tesla valve; liquid cold plate; NCGA algorithm; multi-objective optimization design

check for updates

Citation: Fan, Y.; Wang, Z.; Xiong, X.; Panchal, S.; Fraser, R.; Fowler, M. Multi-Objective Optimization Design and Experimental Investigation for a Prismatic Lithium-Ion Battery Integrated with a Multi-Stage Tesla Valve-Based Cold Plate. *Processes* **2023**, *11*, 1618. https://doi.org/10.3390/pr11061618

Academic Editors: Rosenberg J. Romero and Jesús Cerezo Román

Received: 26 April 2023
Revised: 20 May 2023
Accepted: 23 May 2023
Published: 25 May 2023

1. Introduction

In recent years, there has been global energy reduction and environmental protection requirements to improve the rapid development of electric vehicles (EVs). Among many kinds of power batteries, the lithium-ion battery has attracted increasingly more attention because of its advantages, such as high energy density, low self-discharge rate, and long cycle life. However, the heat generated in the charging and discharging process of lithium-ion batteries will affect the working performance of the battery. Too high a temperature will shorten the service life of the battery and may cause the battery to have thermal runaway or even an explosion [1]. This is also one of the problems that must be solved in the design and manufacture of EVs. Generally, the ideal operating temperature range of lithium-ion batteries is 20–45 °C, and the local surface standard deviation between the battery pack should generally be less than 5 °C [2]. Therefore, building a battery thermal management system (BTMS) with excellent performance and ensuring that lithium-ion batteries work in a proper temperature range is a prerequisite for ensuring the power performance and safety of EVs [3].

Currently, the research on battery thermal management systems is mainly focused on heat dissipation. The common cooling methods include forced air cooling, liquid cooling, phase change material (PCM) cooling, and heat pipe cooling [4]. The active indirect liquid cooling, as the mainstream battery thermal management system cooling solution, relies on the flow of coolant (e.g., water or water/glycol) into metal plates (internal flow channels called cold plates) to remove heat from the battery. Since the cold plate structure parameters have a large impact on the efficiency of the whole cooling system, the existing literature review reports mainly focus on many studies on different structures of cold plates using numerical analysis or algorithmic optimization design. Guo et al. [5] used numerical simulation and an orthogonal test of multiple indexes to optimize the structural parameters and flow rates of the parallel-spiral serpentine channel liquid cooling plate. The result indicates that the flow rate is the main factor affecting the maximum temperature as well as the temperature distribution, while the channel height has a strong influence on the pressure drop. Huang et al. [6] carried out numerical analysis on the cooling plate structure adopted when an actual battery module is undertaken and verified this by comparison with the experiment. On the basis of the thermal characteristics of the battery pack, three structural design schemes for the cooling plate were proposed and analyzed. Compared to the original design, the maximum field synergy angle was reduced by 7.25%, while the cooling efficiency factor was increased by 10.82% for the uneven heating condition of the battery pack. Xie et al. [7] proposed a simple cooling structure with a precisely tailored liquid cooling plate for the thermal management of a large battery module. When there is an aluminum plate thickness of 4 mm and an inlet velocity of 0.275 m·s^{-1}, the maximum temperature and maximum temperature difference of the battery module can be controlled below 31.80 and 3.70 °C, respectively. Li et al. [8] used the response surface methodology (RSM) and non-dominated sorting genetic algorithm (NSGA-II) for multi-objective optimization of a mini U-channel cold plate with SiO_2 nanofluid to obtain the best performance. According to the Pareto optimal solution, the optimal objective functions were T_{max} = 299.42 K, ΔT = 2.66 K, and ΔP = 436.19 Pa. Zhai et al. [9] proposed a novel flow arrangement of staggered flow (the fluid staggers flow along each layer) to remove higher heat flux and obtain a more uniform bottom temperature in double-layered microchannel heat sinks. Compared to the counter flow, the heat transfer performance of two types of staggered flow was studied numerically. The distribution of total temperature, average bottom temperature, maximum temperature difference, and thermal resistance were presented for different flow arrangements under similar pumping power.

Obviously, the current main literature reports focus on the total thermal resistance and surface standard deviation as the two indexes of optimization of cold plate evaluation. The total thermal resistance indicates how much heat a radiator can carry away at a given surface standard deviation. However, it cannot evaluate the temperature uniformity of the battery. In addition, pump power usually increases when thermal resistance decreases. However, high inlet speed or high flow rate is a great challenge to drive pump loss [10]. This shows that it can only improve the heat transfer performance without considering the flow rate of the coolant, thus reducing the driving coolant pump dissipation efficiency and seriously affecting the temperature consistency of the battery module.

However, with the development of microelectronic heat dissipation components towards miniaturization and integration, their weight and size have always been a concern. Among them, the thermal conductive components with microchannel low flow resistance enhanced temperature control function are also widely used, and their thermal performance and pumping power consumption effect is far more than the level of conventional cooling means can achieve. Compared to the previous analysis of the current state of research, being based on Murray's law [11] and Bejan et al.'s [12] construction theory, the cold plate with microchannel structure was found to have a lower flow resistance and a more uniform temperature distribution on the heat dissipation surface, requiring less pumping energy. Moreover, similar design methods have been used in the battery thermal management system to promote a uniform temperature distribution in the battery module, thus avoiding thermal stress concentration and ensuring the efficiency of the overall battery module. He et al. [13] proposed a double-layered I-shaped liquid cooling plate to optimize the operating temperature of a 40Ah $LiFePO_4$ battery using the design idea of construction theory. The optimized I-shaped liquid cooling plate can reduce the maximum temperature from 307.02 to 303.94 K and the standard deviation of surface temperature from 0.80 K to 0.25 K. In addition, the pressure drop was reduced by 73.36% compared to that in the serpentine channel. Qi et al. [14] proposed a Swiss-roll-type liquid cooling micro-channel to cope with the use of battery modules under high-rate discharge conditions. Compared with the serpentine flow channel BTMS optimized by other researchers, the maximum temperature and temperature difference of the Swiss roll battery module and the height of the cooling belt were reduced by 1.2 K and 0.2 K, respectively. Wu et al. [15] designed a microchannel flat-tube-assisted composite silica gel (CSG-LC) to improve the thermal uniformity and thermal stability performance of traditional cooling plates. It was found that the maximum temperature and maximum temperature difference could be controlled below 44.5 and 4.5 °C at a 3 C discharge rate, respectively.

On the basis of the above literature review, micro- or sub-micro-channels were used in the context of BTMS [16]. It has been widely reported that heat sinks with microchannels are commonly used to enhance the cooling of high heat flow regions [17]. To further challenge the heat transfer capacity of microchannels and the resulting pressure drop loss [18], new or refining existing microchannel design features are often used. Among them, the traditional Tesla valve is a typical improved fluid control system used to increase the mass transmission or heat transfer capacity of the system [19]. For instance, Sun et al. [20] designed microchannel heat sinks imitating the Tesla valve (MCTV), mounted with a sector bump (MCSB) and diamond bump (MCDB). The results show that the Nu of MCTV, MCSB, and MCDB were increased by 102.3%, 111.2%, and 94.8%, while the f of these structures were increased by 3.21 times, 3.14 times, and 2.81 times with a *Re* of 800, respectively. Bao et al. [21] proposed two improved parameters (relative pressure drop ratio and absolute pressure drop ratio) in order to make up for defect of diodicity. In addition, a novel Tesla valve with a special tapering/widening structure was designed, analyzed, and compared with other types of Tesla valves, showing a superior absolute pressure drop ratio. At the same time, the heat transfer performance of the Tesla valve was fully investigated, and the maximum temperature difference between forward and reverse flows can be 12.10 K, which has the potential to realize a new way for real-time thermal management. Li et al. [22] designed a 3D Tesla valve manifold two-phase cold plate for a SiC power device module. Through the cold plate top surface temperature distribution measurements, the temperature uniformity of each SiC diode on the Tesla valve cold plate could be maintained at ±5 °C.

Considering the aforementioned research works, it is understandable that most of the literature focuses on improving the existing channel layout and modifying the design features. Conversely, the temperature gradient is still greater than 5 °C as there exists a limitation in heat transfer coefficient enhancement. Unlike the formerly employed channel designs, the present work suggests a novel liquid cooling channel plate by utilizing the Tesla valve design that has grown to prominence in microfluidics, micro-pumps, microelectronics, fuel cell, and heat pipe systems. In addition, on the basis of our previous studies [23] on the flow direction of the Tesla valve, the heat transfer enhancement capability of the reverse flow is mainly caused by pressure duality caused by flow bifurcation, stagnation, and mixing mechanisms [24].

Therefore, this work aimed to design a new cold plate with the MSTV channel, relying on the heat transfer characteristics of the reverse flow of the Tesla valve channel. A high-precision battery thermal model was established through thermal characteristic experiments to provide a reference for the research of cooling system. Secondly, the performance optimization of MSTV-BTMS was carried out using the DoE, Kriging, and NCGA optimization algorithm framework. Factors affecting cell temperature such as coolant volume fraction and valve distance of MSTV channels and coolant inlet velocity, as well as the required pumping power of the cold plate, were included. A liquid cooling system with low temperature and low energy consumption was developed. Finally, the optimization results were verified by a combination of prototype experiments and numerical simulations of the cold plate, and these were compared with the performance evaluation of a traditional serpentine channel with the same heat transfer area.

2. Methodology

2.1. Model Description

2.1.1. Geometric Structure of Cold Plates

Figure 1a shows the assembly scheme of MSTV-BTMS. A prismatic lithium-ion battery (anode: Li $(Ni_{1/3}Co_{1/3}Mn_{1/3})$ O_2, cathode: graphite) was used in this study. The nominal battery capacity was 12Ah, and the dimensions were ($L_x \times L_y \times L_z$) 142 × 65 × 17 mm. The basic parameters of the battery are listed in Table 1. Each battery was placed between two adjacent cold plates, forming a sandwich structure. The sides of the cold plate were closely connected to the battery surface, which facilitated the compact layout of the cooling system. In addition, the D-valve design dimensions were as proposed by De Vries S F et al. [25]. As shown in Figure 1b, the cold plate with the MSTV channel (number of stages $N = 5$) was designed on the basis of a single D-type Tesla valve in series. Since the MSTV channel was placed in a cold plate with limited space, its limit machining allowance was set to R_x. The spacing between MSTV channels was controlled by the valve distance (G). The detailed dimensions and thermal physical parameters of the cold plate with MSTV channels are shown in Table 2. As shown in Figure 1c, the coolant was water, which flowed through the cold plate through the Tesla valve channel to exchange heat with the battery and reduce the battery temperature.

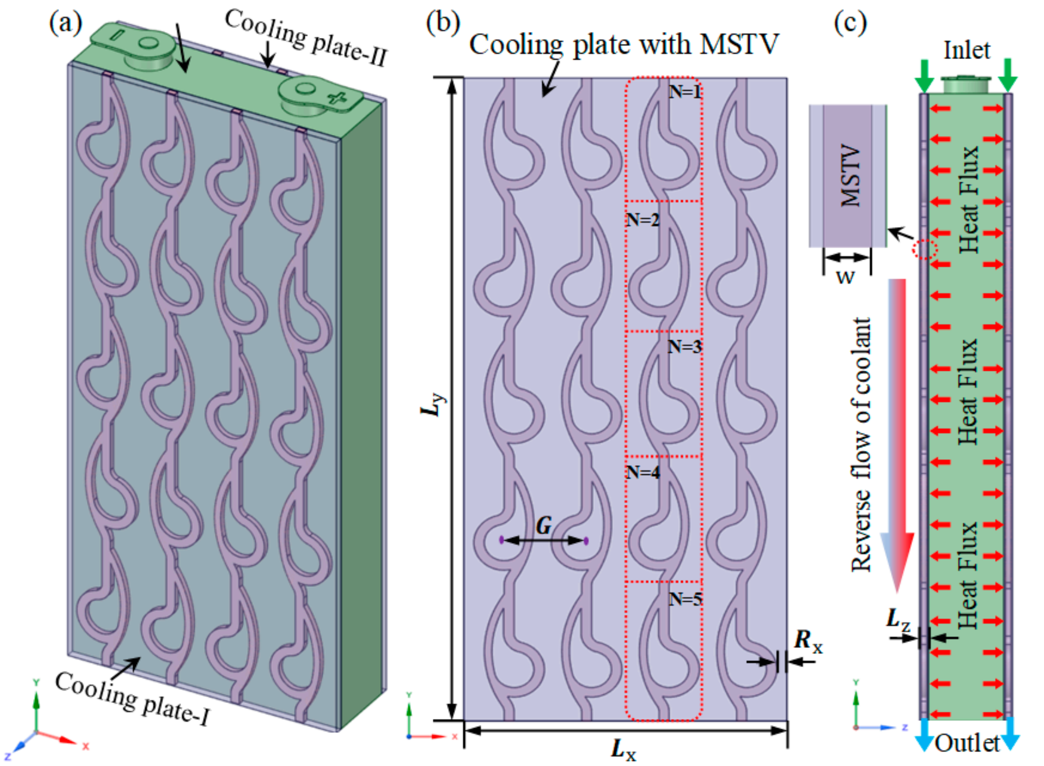

Figure 1. Design of MSTV-BTMS: (**a**) cold plate with MSTV; (**b**) design parameters of the cold plate with Tesla valve-type channels; (**c**) CFD model of the MSTV channel.

Table 1. The 12 Ah prismatic lithium-ion battery parameters.

Parameter	Value	Parameter	Value
Nominal capacity (Ah)	12	Discharge cut-off voltage (V)	2.75
Nominal voltage (V)	3.65	Over-charge protection voltage (V)	4.2
Length (mm)	142	Max discharge current (A)	20
Width (mm)	65	Operating temperature (°C)	0–45
Thickness (mm)	17	Storage temperature (°C)	−20–60
Weight (g)	320	Circle life at room temperature (°C)	1000
Internal resistance (mΩ)	4		

Table 2. Design of the cold plate parameters with the MSTV channel.

Specification	Value
Liquid cold plate	-
Plate length (mm)	142
Plate width (mm)	65
Plate thickness (mm)	2
D-valve dimensions [25]	-
Channel width, d (mm)	2
Channel thickness, W (mm)	0.2–1.8
Valve distance, G (mm)	11.7–15.56
Number of stages, N	5
Density of aluminum channel (kg·m^{-3})	2700
Heat capacity of aluminum channel (J·kg^{-1}·K^{-1})	900
Thermal conductivity of aluminum channel (W·m^{-1}·K^{-1})	238

2.1.2. Construction of the Lithium-Ion Battery Thermal Model

Experimental Set-Up

The experimental settings are shown in Figure 2. The test bench consisted of five components: (1) PC (data transmission of battery surface temperature sensor); (2) temperature measuring device (Tad 6407, Dongguan Kelian Electronics Co., Ltd., Dongguan, China); (3) battery management system (EVTS-LNR-60V-100A-4ch, Arbin, Ltd., College Station, TX, USA); (4) temperature control box (KCS-8900B, Wuhan Environmental Testing Equipment Co., Ltd., Wuhan, China); (5) prismatic lithium-ion battery (China Aviation Lithium Battery Co., Ltd., Wuhan, China). The accuracy of each instrument is shown in Table 3.

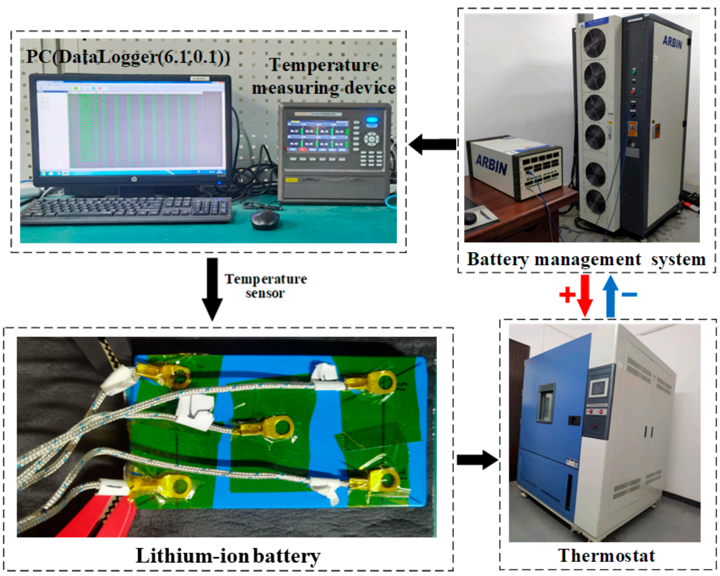

Figure 2. Experimental set-up for battery module thermal characterization.

Table 3. Range and accuracy of related instruments in the experiment.

Experimental Instruments	Range	Accuracy
Temperature measuring device (TAD-6407)	−200∼600 °C	±0.2% FS
Battery management system (EVTS-LNR-60V-100A-4ch)	2∼60 V 0∼100 A	±0.1% FS
Temperature control box (KCS-8900B)	−43~120 °C 1 m × 1 m × 1 m	±0.5 °C
Temperature sensor (k-type)	−50∼260 °C	±0.15 °C

Obtaining the Thermodynamic Parameters of a Battery

In this work, a commercially available prismatic lithium-ion battery (anode: Li ($Ni_{1/3}Co_{1/3}Mn_{1/3}$) O_2, cathode: graphite) was investigated. The specific battery specification parameters were as shown in Table 1. In the numerical solution, the physical parameters of the battery included density (ρ_b), thermal conductivity (k_b), and specific heat capacity (C_b). For simplicity, the battery consisted of a single material, so ρ_b, k_b, and C_b were constants. According to the mass m_b and volume V_b of the battery, the density V_b of the battery was calculated to be 2220.8 kg/m^3 ($\rho_b = m_\mathrm{b}/V_b$).

Since the thermodynamic behavior of the battery is closely related to its electrochemical reaction, the thermal conductivity (k_b) of the battery was assumed to be anisotropic in the current simulation [26]. This behavior, highlighted by Drake et al. [27], has implications for design and modeling strategies. However, the thermal conductivity of a prismatic lithium-ion battery was negligible along the thickness direction compared to the planar direction. Considering the geometric and thermophysical characteristics of the structure, the thermal conductivity of the prismatic cell was calculated as follows [28]:

$$k_{b,x} = \frac{\sum(l_i \cdot k_{T,i})}{\sum l_i} \tag{1}$$

$$k_{b,y} = \frac{\sum l_i}{\sum \frac{l_i}{k_{T,i}}} \tag{2}$$

where i represents the index of the structural part, and $k_{b,x}$ and $k_{b,y}$ represent the thermal conductivity of different direction. Thus, the thermal conductivity of the lithium-ion battery was set, as shown in Table 4.

Table 4. Thermodynamic parameters of the battery.

Parameter	Value
$\rho_b\left(\mathrm{kg \cdot m^{-3}}\right)$	2220.8
$k_b(\mathrm{W \cdot m^{-1} \cdot K^{-1}})$	0.63 [29] (Plane direction; Thickness direction: Negligible)
$C_p\left(\mathrm{J \cdot kg^{-1} \cdot K^{-1}}\right)$	1399.1

In the study of thermodynamic and physical parameters, Bernardi [30] proposed a set of methods for measuring the heating power and specific heat capacity of lithium-ion batteries. This method does not require complex equipment and is easy to implement [31]. As shown in Figure 3a, the lithium-ion battery to be tested was wrapped under cotton bale insulation conditions, while insulating Kapton tape was applied to ensure that the lithium-ion battery was in a relatively insulated environment within the thermostat to complete the experiment. The K-type thermocouples were calibrated by an ice water mixture in a vacuum bottle to ensure the difference between the measured value and the real value was within 0.1 °C.

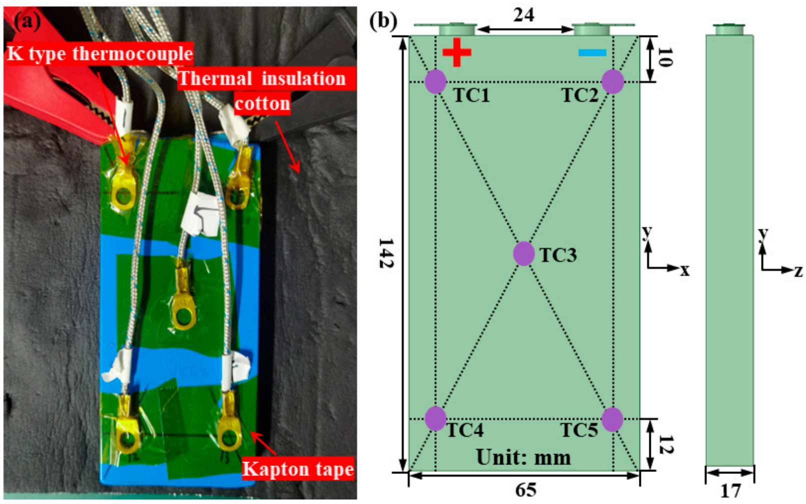

Figure 3. Thermocouple locations and physical dimensions: (**a**) picture of thermocouple locations; (**b**) physical dimensions.

Moreover, the heat generated from different locations of lithium-ion batteries varies greatly. Therefore, it is recommended to arrange the temperature sensors as in the previous experiment by Panchal et al. [32]. In this study, five K-type thermocouples were placed in different locations; as shown in Figure 3b, the first thermocouple (TC1) was placed near the anode, the second thermocouple (TC2) was near the cathode, the third thermocouple was on the middle surface of the cell (TC3), and the fourth (TC4) and fifth thermocouples (TC5) were placed on the bottom side of the cell.

The heat generated by a battery (q_{gen}) is mainly composed of two parts. One is the irreversible heat generated by the internal resistance of the battery, and the other is the reversible heat generated by the electrochemical reaction inside the battery. In addition, according to the typical Bernadi heat generation model [30], the heat generated by the battery (q_{gen}) is equal to the heat absorbed by the battery (q_{abs}) in an insulated environment.

$$q_{gen} = I^2 R_j + I T_b \frac{\partial U_{ocv}}{\partial T_b} \tag{3}$$

$$q_{abs} = m_b c_b \frac{dT_b}{dt} \tag{4}$$

After transforming Equations (14) and (15), Equation (16) can be obtained.

$$\frac{1}{I}\frac{dT_b}{dt} = \frac{R_j}{m_b c_b} \cdot I + \frac{1}{m_b c_b} \cdot T_b \cdot \frac{\partial U_{ocv}}{\partial T_b} \tag{5}$$

To insulate the battery, the battery to be tested was placed in the incubator, as shown in Figure 3. Discharge was at four different rates (1 C, 2 C, 3 C, and 4 C). Refer to our previous research basis [33]. Therefore, function $\frac{1}{I}\frac{dT_b}{dt}$ can be regarded as the linear relationship of current I in Equation (6), and the linear relationship between $\frac{1}{I}\frac{dT_b}{dt}$ and I can be obtained by experiments, as shown in Figure 4.

The linear equation is as follows:

$$\frac{1}{I}\frac{dT_b}{dt} = 7.9 \times 10^{-6} I - 1.76 \times 10^{-5} \tag{6}$$

According to Equation (17), the slope of the line is $\frac{R_j}{m_{lb} c_b}$, and the equivalent specific heat (C_b) of the battery is 1399.1 J/(kg·K).

Finally, in an adiabatic environment of 30 °C, the heating power of the battery was calculated by Equation (7).

$$q_{gen} = q_{abs} = m_b c_b \frac{dT_b}{dt} \tag{7}$$

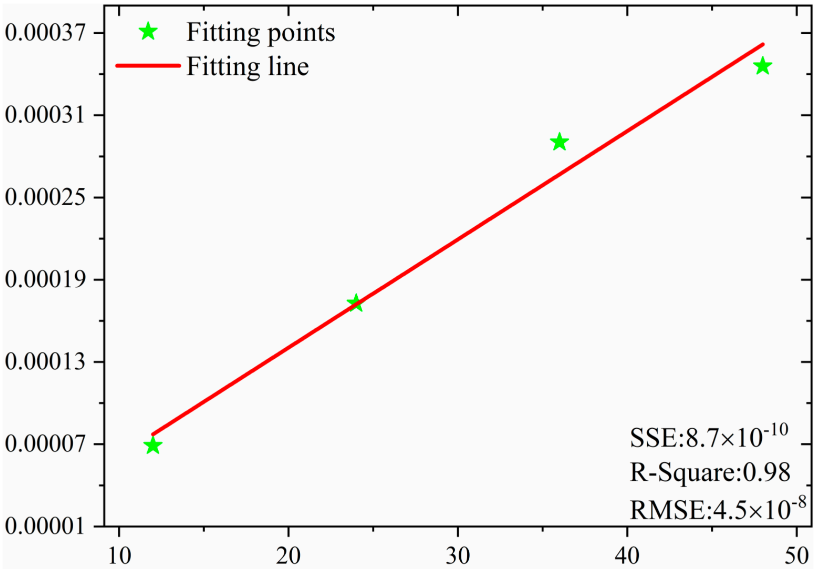

Figure 4. Experimental fitting results.

2.2. The Governing Equations

The computing domains included the coolant, cold plate, and battery. To simplify the calculation, the cold plate was assumed to be homogeneous and isotropic before the simulation. The coolant was a single laminar flow and incompressible. We neglected the radiative heat transfer from the external housing of the cell and cold plate.

On the basis of the above assumptions, the governing equations of different subdomains are [7]:

(1) For the coolant, the mass conservation is as follows:

$$\nabla\left(\rho_c \vec{v}\right) = 0 \tag{8}$$

Energy conservation in the fluid domain:

$$u\nabla T = \frac{K_c}{\rho_c C_c}\nabla^2 T \tag{9}$$

In addition, momentum conservation of the coolant can be expressed as

$$(u\cdot\nabla)\rho_c \vec{v} = -\nabla p + \mu\nabla^2\vec{v} \tag{10}$$

(2) In the solid region of the cold plate, the energy equation is expressed as

$$\nabla^2 T = 0 \tag{11}$$

where ρ_c is the density of the coolant; $\vec{v}$ is the coolant velocity vector; p is static pressure of the coolant; μ is the dynamic viscosity; K_c is thermal conductivity of the coolant; and C_c is specific heat capacity of the coolant.

(3) For the lithium-ion battery module, the energy conservation equation can be written as [23]

$$\rho_b C_{p,b} \frac{\partial T_b}{\partial T_t} = \nabla \cdot (k_b \nabla T_b) + q_{gen} \tag{12}$$

where ρ_b, k_b, and T_b are the density, thermal conductivity, and temperature of the battery, respectively. q_{gen} is the total heat produced by the battery.

2.3. Boundary and Initial Conditions

In this study, the anisotropy of the internal conductivity of the cell was considered. Therefore, using the commercial software ANSYS FLUENT in the numerical simulation, the battery was defined as a time-varying heat source rather than the surface heat flow boundary, and the temperature of the entire cross-section of the battery can be calculated. Moreover, through the follow-up experiment, the simulation process was set as the heat production rate with different discharge rates. In this process, UDF (user-defined function) was used to define the thermal source (lithium-ion battery). The boundary conditions were set as follows:

(1) Interface coupling conditions of the lithium-ion battery and liquid coolant [5]:

$$-k_b \frac{\partial T}{\partial n} = -k_{MSTV} \frac{\partial T}{\partial n} \tag{13}$$

where k_b is the thermal conductivity of the battery, and $\partial T / \partial n$ is the temperature gradient.

(2) The boundary conditions of the interface between the solid area (aluminum) of the cold plate and the liquid coolant are defined as follows [23]:

$$-k_{MSTV} \frac{\partial T}{\partial n} = -k_c \frac{\partial T}{\partial n} + h_c (T_c - T_{MSTV}) \tag{14}$$

where k_{MSTV} is the surface temperature of the internal channel, h_c is the heat transfer coefficient of the liquid coolant, T_c is the temperature of the coolant, and T_{MSTV} is the surface temperature of the internal channel.

In addition to the boundary of the cooling system, the relevant initial conditions were given:

- Inlet: Coolant flow rate at each inlet is defined as V_c. The initial temperature of coolant and ambient air is maintained at 30 °C. Equation (15) provides the inlet velocity of the cross-sectional area of the coolant from 75 to 300. The definition is as follows [18]:

$$V_c = \frac{R_e \mu_{cl}}{\rho_c D_h} \tag{15}$$

$$D_h = \frac{4 A_{ch}}{P} \tag{16}$$

where μ_{cl} is the viscosity of coolant; D_h is the inlet hydraulic diameter; A_{ch} is the cross-sectional area of the MSTV channel; and P is the perimeter inlet of the MSTV channel.

- Outlet: Take the environmental pressure as the reference pressure of the outlet fluid, equal to 0 Pa.
- Wall: The upper and lower walls of the cold plate close to the lithium-ion battery are conjugate heat transfer walls. The other walls are assumed to be adiabatic. According to Equation (15), the inlet Reynolds number (*Re*) of the cooling system is less than 300. Therefore, the fluid flow is laminar in this case [18]. The SIMPLEC algorithm is adopted for the second-order and third-order equations.

2.4. Model Rationality Demonstration

2.4.1. Grid Independence Verification

In this study, the pressure drop (ΔP) of the MSTV channel, the maximum temperature (T_{max}), and the surface standard deviation (T_{σ}) of the cell were used as performance evaluation metrics for MSTV-BTMS, where the pressure drop of the MSTV channel indicated the pumping power consumption undertaken by the coolant to remove the heat from the lithium-ion battery. The maximum temperature (T_{max}) of the cooling system can embody the worst working condition of the battery. The surface standard deviation (T_{σ}) indirectly indicates that the temperature distribution of the battery is uniform. The smaller the standard deviation of the surface, the more uniform the temperature distribution of the battery [34]. The surface standard deviation (T_{σ}) can be computed as follows [13]:

$$\overline{T} = \frac{\int_{A_0} TdA}{\int_{A_0} dA} \tag{17}$$

$$T_{\sigma} = \sqrt{\frac{\int_{A_0} \left(T - \overline{T}\right)^2 dA}{\int_{A_0} dA}} \tag{18}$$

The cold plate of the initial design was embedded with four MSTV channels. The initial width and depth of the channels were pre-set to 2 mm and 1 mm, respectively. A poly-hexcore grid was used for the grid construction (Figure 5a), and three bundles of 416,409, 531,931, and 777,108 grid cells were finally obtained for sensitivity analysis. Figure 5a shows the response of the pressure drop (ΔP) of the MSTV channel, the maximum temperature (T_{max}), and the surface standard deviation (T_{σ}) of the cell. It can be seen that there was hardly any difference between the predictions with different grid resolutions.

Therefore, as shown in Figure 5b, the grid structure was used in this study. Its generation strategy was to transition from surface grid to volume grid. It consisted of 416,409 individual grids, 28,836 boundary grids, and 90,004 nodes. The overall cell size of the surface grid was controlled as the minimum size of 0.12mm and the maximum size of 2 mm. The growth rate was 1.2. The size functions were curvature and proximity type. The curvature normal angle was 18°. Volume grids were generated as poly-hexcore types. The buffer layers were 2 in number, and the peel layer was 1 in number. The max cell length did not exceed 11.5. The minimum cell quality was 0.215, and the average cell quality was 0.547. The maximum-skewness was 0.633, and the maximum aspect ratio was 0.614. The channel region consisted of 156,973 poly cells. The minimum cell quality was 0.351, and the average cell quality was 0.677. The maximum aspect ratio was 0.7548, and the maximum aspect ratio was 0.5. In addition, on the basis of engineering experience, the whole model was built around three boundary layers with a total thickness of 0.036 mm in the fluid and solid connection area.

2.4.2. Model Rationality Demonstration

It is well known that lithium-ion batteries can transfer heat through natural convection in their shell during charge and discharge tests, especially during high-rate (more than 2C) discharge operations [35]. Generally, the convective heat transfer coefficient (h_b) under natural conditions usually ranges from 6 W·m^{-1}·K^{-1} to 10 W·m^{-1}·K^{-1} [36]. In this work, the appropriate value of h_b was not only to improve the heat dissipation of the battery but also directly affected the accuracy of the battery thermal model during the simulation.

To better capture the convective heat transfer characteristics of the cell surface, three-dimensional numerical simulations were performed using the cell heat production rate tested at 4C discharge multiplier conditions. The different convection coefficients were pre-set in each simulation, and the average temperature profile of the simulated cell was fitted to the experimental results. As shown in Figure 6a, the different values of h_b were obtained. It can be clearly found that the value varied with the depth of discharge of the lithium-ion battery due to the pre-setting of different convection coefficients. In this work, the maximum deviation between the simulated and experimental results was 2.9% when h_b = 8 W·m^{-1}·K^{-1} and in much less than 5% [35]. This indicated that the convection coefficients obtained for the cell surface were reliable.

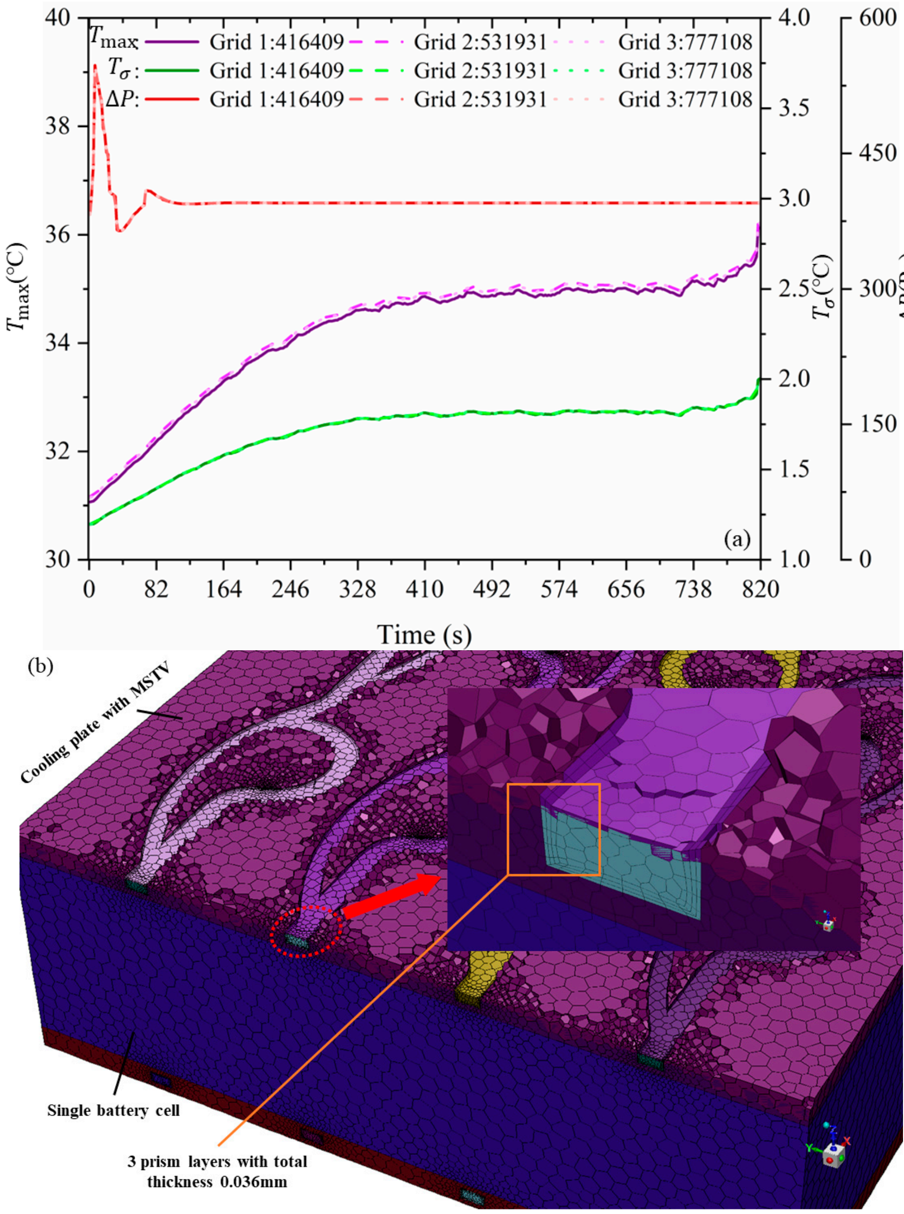

Figure 5. Grid independence verification: (**a**) the influence of grid number on pressure drop (ΔP), maximum temperature (T_{max}), and surface standard deviation (T_σ); (**b**) CFD model with a geometric shape system.

Therefore, in this work, to simplify the model development, the actual temperature variation of the battery thermal model was verified by choosing h_b = 8 W·m^{-1}·K^{-1}, as shown in Figure 6b. The results showed that the simulation results agreed well with the experimental results, with a maximum relative error of less than 1.4 °C. The experimental results showed that the method of calculating the heat production rate of the battery was accurate. The developed thermal model of the cell was sufficient to describe its transient thermal behavior.

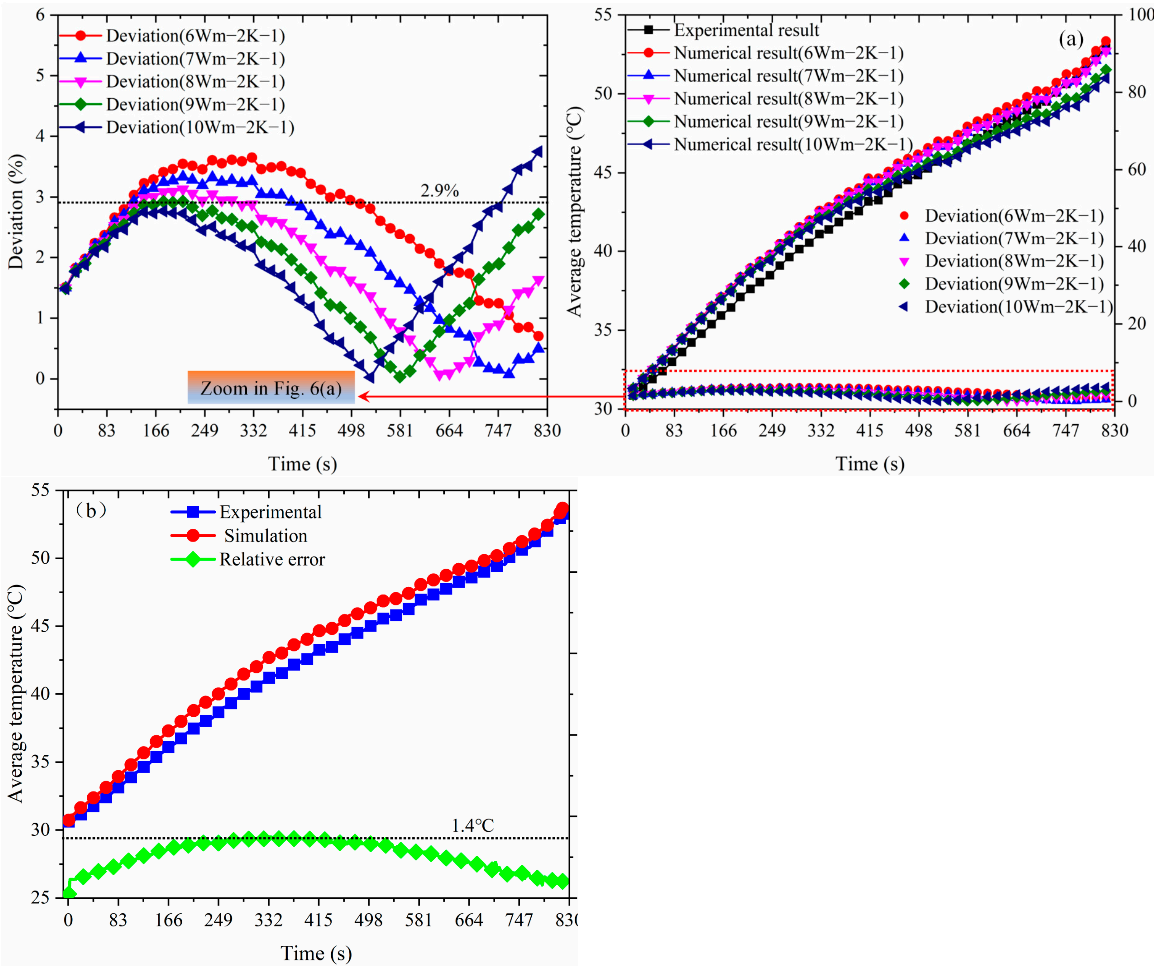

Figure 6. Error comparison between experimental and measured values under different convective coefficients at a 4C discharge rate: (**a**) temperature of different convective coefficients; (**b**) simulation and experimental comparison.

3. Performance Analysis of the Initial MSTV Geometry

The main purpose of this work was to develop a cooling system with good cooling performance and low pump energy consumption. In addition, it was considered that the Tesla valve was a passive operation and had a no-moving-parts design. Moreover, the design size of its body structure was basically fixed. Therefore, in this work, the research of novel design MSTV-BTMS was mainly divided into three parts:

(1) The MSTV channel was formed on the basis of a single Tesla valve in series, and the initial cold plate structure was constructed. Through the finite space arrangement of the cold plate, the influence of the volume fraction of liquid coolant (μ_c) and valve distance (G) on the heat removal performance of the cold plate was preset.

(2) Further, we selected the multi-objective optimization (the DoE, Kriging, and NCGA optimization algorithm framework) by the liquid cooling system optimization scheme. The optimal structure of the MSTV was also explored.

(3) The superiority of the MSTV structure (cooling performance, pumping energy consumption) was verified experimentally. The cooling performance was also compared with that of a conventional serpentine channel at the same heat transfer area.

3.1. Influence of the Coolant Volume Fraction on the Cooling Performance

The coolant volume fraction (μ_c) refers to the ratio of the volume of the cooling channel to that of the cold plate. For example, Ghaedamini et al. [37] set the channel volume fraction between 0.05 and 0.1, and the cooling device achieved the best heat removal performance.

However, in this work, the overall size of the cold plate effects and the individual D-valves had a fixed size. Therefore, the designer considered arranging different numbers of MSTV channels inside the cooling plate with a view to obtaining different coolant volume fractions. In the design space, the maximum coolant volume fraction was calculated to be about 0.135 (four channels). As shown in Table 5, the final volume fraction was therefore pre-set to 0.030 (one channel), 0.063 (two channels), 0.098 (three channels), and 0.135 (four channels).

Table 5. Comparison of the cold plate performance with a volume fraction of the coolant when *Re* = 300.

Design	μ_c = 0.030	μ_c = 0.063	μ_c = 0.098	μ_c = 0.135
T_{max} (°C)	37.0	36.1	35.8	35.5
T_{σ} (°C)	1.07	0.92	0.89	0.88

Figure 7 shows all temperature contours of the reverse flow of the MSTV channel along the plane of the cooling plate for *Re* from 75 to 300. It can be clearly noticed that the high thermal stress (red area) on the surface of the cold plate gradually shifted flat to the right as the volume fraction of the coolant increased. The direction of this movement was consistent with the coolant flow direction, which also indicated that different constant flow rates can directly change the heat accumulation problem of the cold plate. If *R*e = 300 and the MSTV channel volume fraction was preset to 0.135, the surface temperature of the cold plate was more uniform (the red area decreases) at this time, and the highest temperature was only 31.2 °C.

All the simulated cases in Figure 7 were further extracted, and the T_{max} and T_{σ} curves of the cold plate were obtained, as shown in Figure 8. When the coolant fraction (μ_c) increased, both the maximum temperature and the surface standard deviation of the cooling plate gradually decreased. Moreover, with the significant effect of *Re*, the lowest T_{max} and T_{σ} were found at this time for the four-channel cold plate.

On the basis of the above extrapolated discussion, it is known that it is crucial to have an optimal channel volume fraction to obtain the best heat transfer performance of the cold plate. As Hung et al. [38] pointed out, the variation of the volume fraction (μ_c) had a negative effect on the mechanical resistance inside the channel. This also indicates that increasing the contact area of the coolant inside the cooling plate had a significant improvement on the convective heat transfer performance of the cell. Therefore, in this study, as shown in Table 5, when μ_c = 0.135 and *Re* = 300, the T_{max} and T_{σ} of the cooling plate were 35.5 °C and 0.88 °C, respectively. Therefore, this research work requires further optimization of the MSTV cooling channel under the constraint of constant volume fraction (μ_c = 0.135).

3.2. The Influence of Valve Distance on the Cooling Performance

In the MSTV channel design, the optimal channel volume fraction was determined to be 0.135, and the number of stages of the channel to be N = 5. Other design dimensions were kept the same, and the valve distances (G) between valves were 11.7, 13.046, 14.3, and 15.56 mm, respectively. Figure 9 shows the evolution of T_{max} and T_{σ} for the reverse flow in the MSTV channel by changing the valve distance. For example, when *Re* was 75 and G changed from 11.7 to 15.56 mm, T_{max} decreased by 3.08 °C and T_{σ} increased by 45.68%. With *Re* increasing to 300, T_{max} decreased by 4.02 °C and T_{σ} increased by 47.3%. These results show that the cooling performance of the cold plate will be greatly improved with the increase in MSTV channel valve distance. In addition, as the flow rate of coolant through the channel became larger, the efficiency for the cooling plate to remove cell heat increased significantly currently. This was mainly because the G value increased the heat transfer area of the cooling plate.

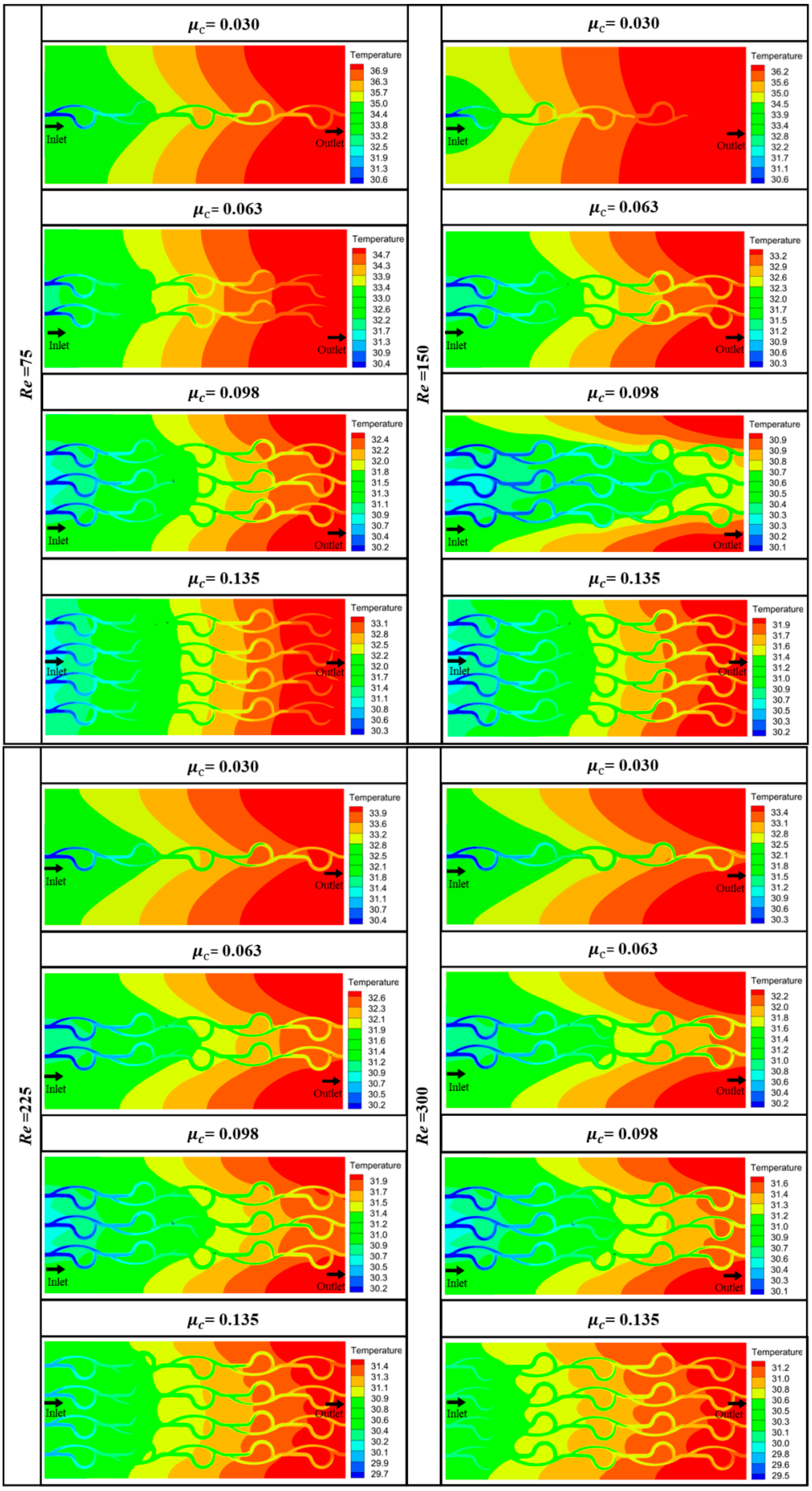

Figure 7. Temperature contours of the MSTV channel (including the cold plate cross section) for *Re* of 75 to 300.

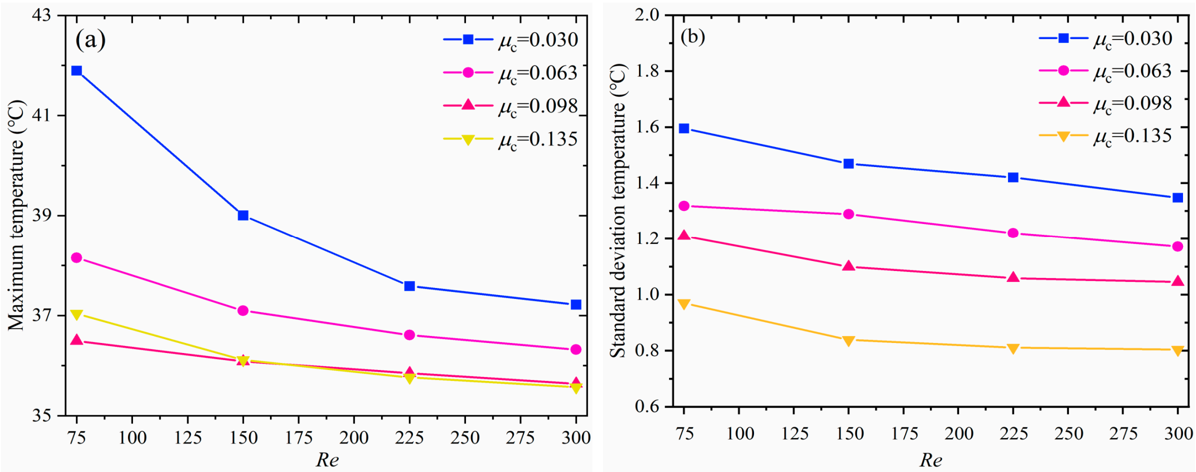

Figure 8. (**a**) T_{max} and (**b**) T_{σ} of the cold plate with MSTV channels as the number of channels varied.

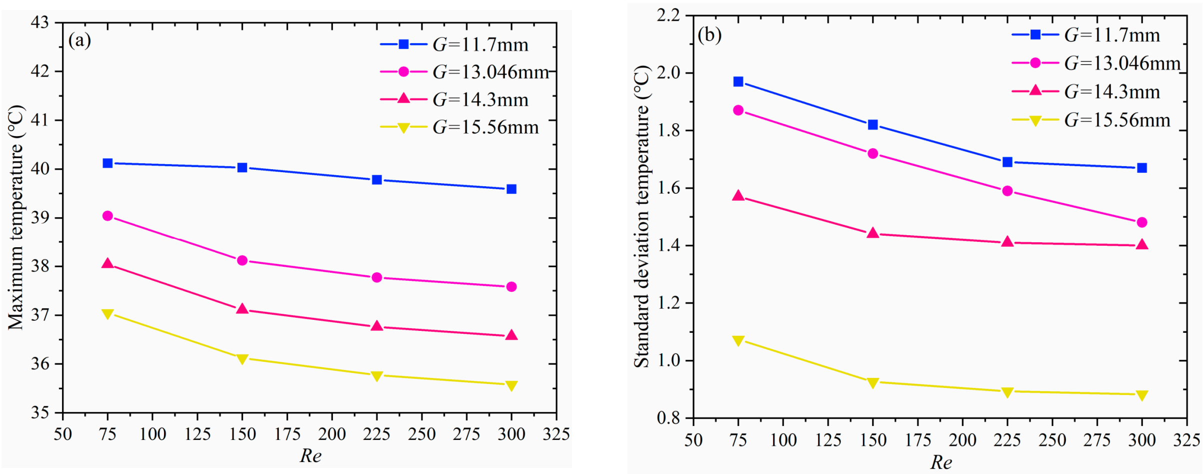

Figure 9. Comparison of (**a**) T_{max} and (**b**) T_{σ} across the four-channeled cold plate with a reverse flow direction in MSTV for varying G.

Figure 10 describes the evolution of the temperature profile of the cooling plate with the variation of the valve distance G at Re of 300. It can be clearly found that the low temperature region of the cooling plate was at the cooling plate inlet position, and the high temperature region was significantly distributed in the coolant outlet region. As the valve distance between the MSTV channels decreased, the heat removal performance of the cold plate gradually decreased. When G = 11.7 mm, the surface temperature of the cold plate was more significant, and T_{max} reached 31.2 °C. When G increased to 14.3 mm, the hot spot quickly contracted to a limited area near the channel exit. Finally, the entire high-temperature region of the cooling plate essentially disappeared at G of 15.56 mm. The low-temperature region was also more uniform along the flow direction. It can be seen that when Re was 300, the volume fraction of coolant was controlled at about 0.135, and the cooling performance of the MSTV channel cooling plate with G of 15.56 mm was more significant.

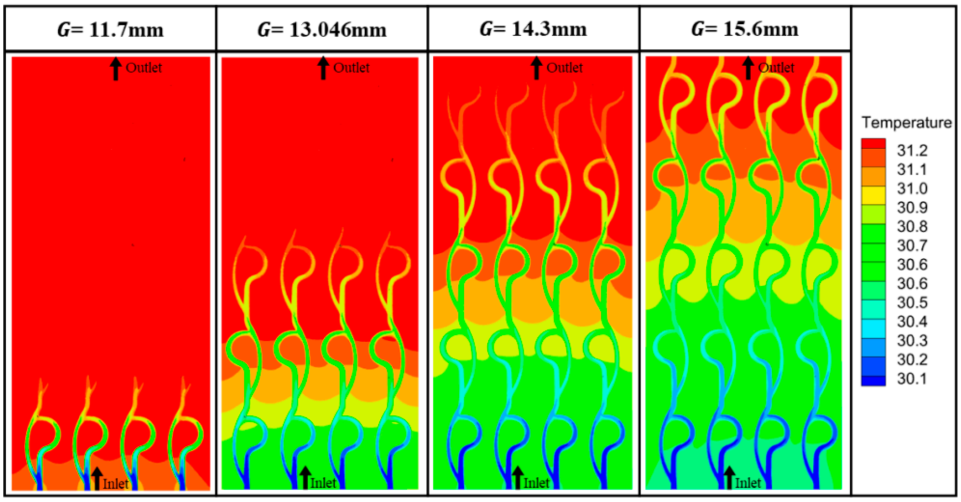

Figure 10. Evolution of temperature contours for a four-channeled cold plate with a reverse flow direction in MSTV at Re of 300 for varying *G*.

4. Multi-Objective Optimization Design

On the basis of the above discussion, it can be found that some design parameters of the MSTV-BTMS directly affected the cooling efficiency and pressure drop. The multi-objective optimized design was carried out by constructing an agent model with the design parameters as input variables. The objectives of the optimized design were the cooling effect, the uniformity of temperature distribution, and the pumping power consumption. One of the multi-objective optimization flowcharts is shown in Figure 11, which was divided into five main steps:

(1) Structure design of MSTV-BTMS.
(2) The sample space was obtained by the DOE method and CFD numerical solution.
(3) The Kriging approximation model was used to establish an approximation model between the design variables and the objective function. Moreover, the robustness of the model was further analyzed.
(4) Optimal design selection using NCGA algorithms.
(5) Experimental verification of the initial design and optimization design.

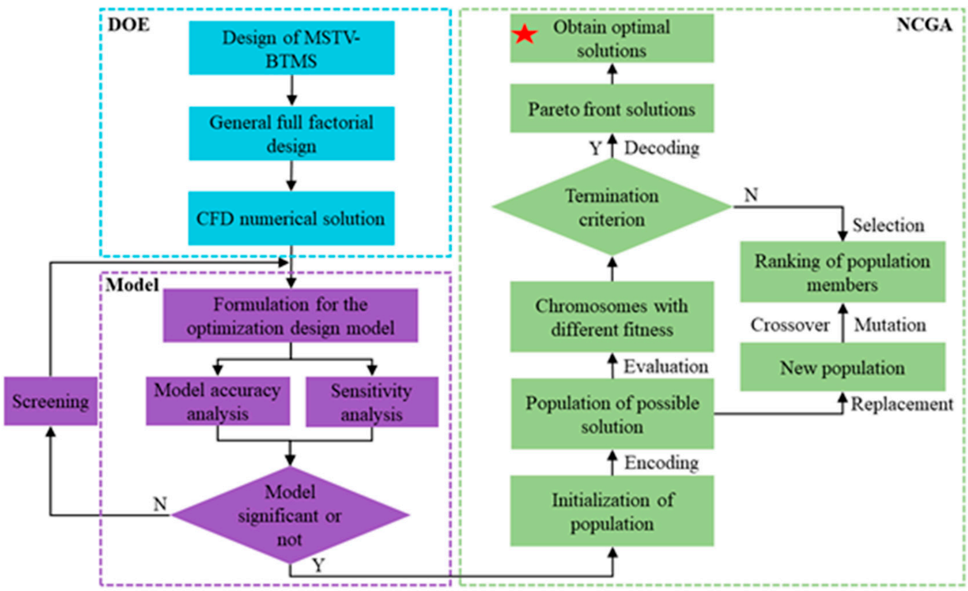

Figure 11. Multi-objective optimization flow chart.

4.1. Optimization process of MSTV-BTMS

(1) General full factorial design

In this study, the effects of the MSTV channel valve to valve distance, thickness, and the coolant velocity on the performance index of the MSTV-BTMS were considered. The general full factorial design scheme was adopted [39], as shown in Table 6. Sample data of the test operation are shown in Appendix A. Each column of the matrix represents a variable, and each row represents a set of test parameters.

Table 6. Design variables and levels.

Level	Design Variables		
	***G* (mm)**	**W (mm)**	***Re***
1	11.7	0.2	75
2	13.046	0.73	150
3	14.3	1.27	225
4	15.56	1.8	300

(2) Kriging approximation model

In the approximate model, it is easy to construct a mathematical model without reducing the computational accuracy, which can reduce the computational cost of performing optimization and simplify the simulation code and analysis. Among the approximation model construction methods, the Kriging approximation model is an unbiased estimation model with minimum estimated variance. A global approximation model valid for the whole design space can be constructed [40]. As a mainstream approximate model, it has been widely used in academic and engineering research. The Kriging model is defined by Equation (19).

$$U(s) = \beta F(s) + z(s) \tag{19}$$

where $U(s)$ is the response function, β is the global regression model, and $z(s)$ is the correlation function. It is a local deviation created on the basis of the regression model with zero mean and non-zero variance [41].

(3) NCGA global search

The neighborhood cultivation genetic algorithm (NCGA) is a modified algorithm of the genetic algorithm with objectives of the same importance. After ranking all objectives, "adjacent propagation" is achieved by crossover, which increases the probability of crossover propagation of solutions close to Pareto on the boundary and speeds up the convergence process [42]. In this study, the MSTV-BTMS structural parameter optimization problem is known to be a complex nonlinear mixed variables problem. Therefore, the NCGA global search is used to solve the above Kriging approximation model. Table 7 shows the initial settings of NCGA. The optimization process of NCGA is shown in Figure 11.

Table 7. The setting of the NCGA basic parameters.

Parameters	Values
Population size	10
Number of generations	20
Crossover type	1
Crossover rate	1.0
Mutation rate	0.01
Gene size	20
Max failed runs	5
Failed run penalty value	1.0×10^{30}
Failed run objective value	1.0×10^{30}

Suppose that $u_1(s) = T_{max}, u_2(s) = T_\sigma, u_3(s) = \Delta P$, the objective function satisfies the following constraints:

$$minU(s_i) = [u_1(s), \quad u_2(s), \quad u_3(s)] \tag{20}$$

$$s.t \begin{cases} s_i = [G, W, Re] \\ 11.7mm \le G \le 15.56mm \\ 0.2mm \le W \le 1.8mm \\ 75 \le Re \le 300 \\ R_x = 2mm \end{cases} \tag{21}$$

where s_i is the design variable vector.

4.2. Robustness analysis of MSTV-BTMS

To ensure the accuracy of the approximation model, 64 sets of directly sampled training samples, shown in Appendix A, were used to construct the metamodel for MSTV-BTMS. In addition, the usual approach of selecting additional sampling points for error analysis was able to be calculated, and the error approximation substituted turned out to be within a reasonable range. Therefore, the Kriging approximation model based on 25 samples of data was provided to test the computation of R^2_{adj} values.

As shown in Figure 12, the 45° diagonal line indicated that the predicted and actual values completely overlapped. The actual and predicted values of the objective functions T_{max}, T_σ, and ΔP were essentially on this diagonal line. The R^2_{adj} values were 0.94, 0.97, and 0.94, respectively. This error result indicates that the approximate model selected in this study had a high confidence level [43], and it can be used for subsequent optimization calculations instead of CFD simulations.

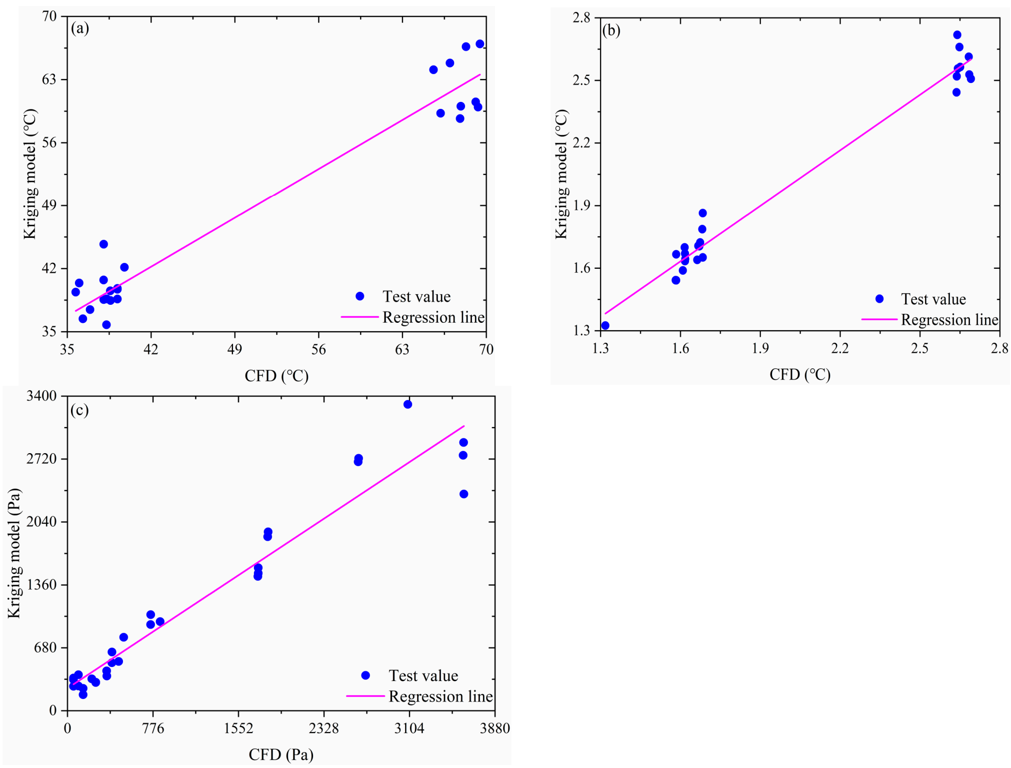

Figure 12. Twenty-five sets of verification parameters set for the objective function: (**a**) T_{max}; (**b**) T_σ; and (**c**) ΔP.

In this work, the sensitivity analysis of MSTV-BTMS under high-rate discharge operation (4C) was performed. To perform a comprehensive analysis of each parameter, the correlation of the parameters was evaluated by linear correlation on the basis of the work of Pearson and Spearman [44].

Figure 13 shows the results of the sensitivity analysis of the design parameters of the MSTV-BTMS with respect to its performance evaluation index. In terms of the maximum temperature of the MSTV-BTMS, the *Re* value of the coolant had the greatest influence (negative correlation was 77%), followed by the MSTV channel valve pitch (positive correlation was 56%), and finally the thickness of the MSTV channel (positive correlation was 44%). The three appeared to be the more significant positive and negative correlations among them. It can hence be seen that when the coolant flow rate through the MSTV cooling plate was larger, the performance for battery heat dissipation was poor at this time. However, proper design of the structural parameters (*G*, W) of the cooling plate can effectively improve the maximum temperature of the lithium-ion battery.

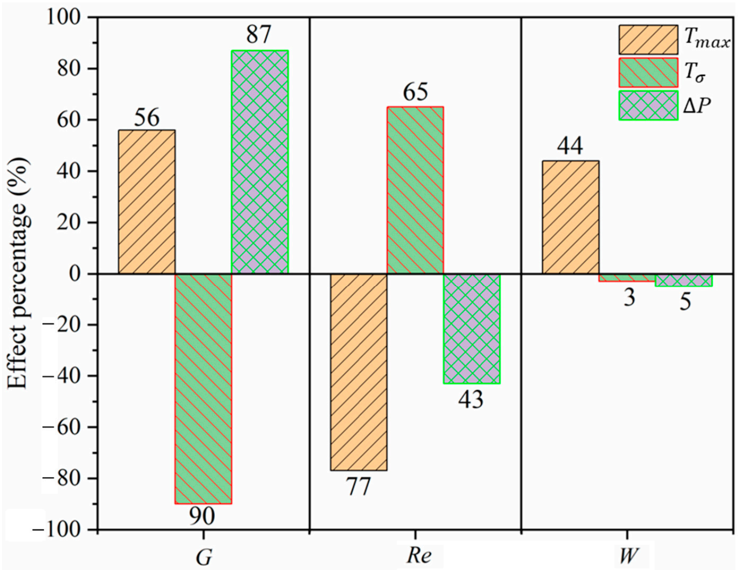

Figure 13. Sensitivity diagram of the impacts of input variables on three objectives.

In terms of the surface standard deviation in MSTV-BTMS, a positive correlation (65%) appeared for T_σ with increasing *Re*. The structural parameters (*G*, W) of the cooling plate were completely opposite for the surface standard deviation, which were −90% and −3%, respectively. It can be clearly found that *Re* and *G* had a greater effect on the ΔP of the cooling plate when evaluating the cooling plate pumping power consumption. Interestingly, proper adjustment of the *G* value of the MSTV channel and the flow rate (*Re*) of the inlet can improve the temperature uniformity of the lithium battery and the power consumption of the cooling plate driving the coolant. However, it needs to be explained that the influence of *G* of the MSTV channel on ΔP of the cold plate is indirect, which may be the interaction between *G*, W, and *Re*, all of which have a better sensitivity to the MSTV-BTMS performance. In other words, this also confirms that the robustness of the nonlinear mixed model based on Kriging's method is fully satisfied with the optimal design of the MSTV-BTMS operating performance parameters. Thus, positive and negative correlations appear between the three design variables, requiring further compromise solutions given by the designer.

4.3. Optimization Design

In this work, on the basis of the established Kriging approximation model, the NCGA optimization algorithm was used to solve the structural parameters of MSTV-BTMS. After 201 iterations, 100 viable solutions were achieved in less than a minute, as shown in Figure 14. All objective functions changed with different design parameters, and there were design parameters corresponding to the optimal objective function. It is usually important to consider that the compromise solutions computed by the NCGA algorithm are all non-inferior solutions when dealing with multi-objective problems. Watanabe [42] considered that it is necessary to represent this with the Pareto optimal solution. To detect the Pareto optimal frontier, the NCGA algorithm is used to calculate the optimal value of MSTV-BTMS again, and finally the T_{max}, T_{σ}, and ΔP were 34.5 °C, 1.58 °C, and 309.59 Pa, respectively. The corresponding design parameters (*G*, W, and *Re*) were 14.79 mm, 0.94 mm, and 243, respectively.

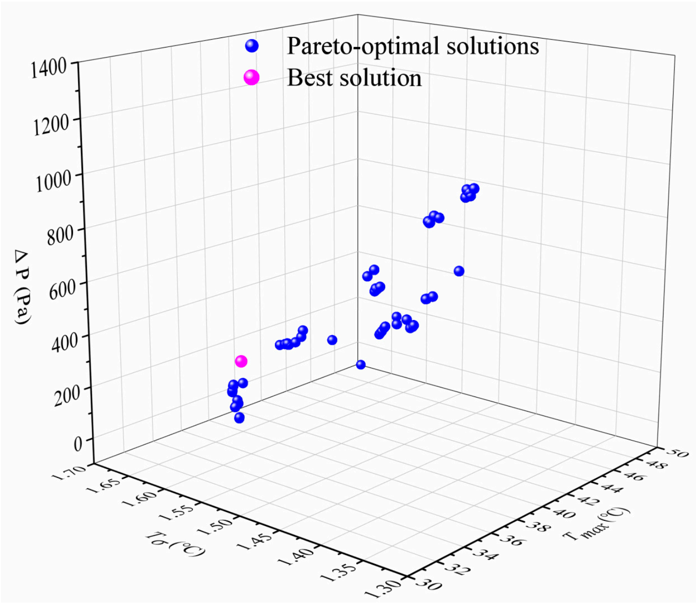

Figure 14. Pareto optimal front for $\mu_c = 0.135$ of T_{max}&T_{σ}&ΔP select ideal point.

5. Experimental Verification and Performance Evaluation

5.1. Experimental Set-Up

The traditional machining method of the micro-channel cold plate is to process the micro-channel and cover plate individually by milling technology. Then, the multiple components are assembled to form a complete liquid cooling system by a bolting or welding process. The disadvantage of this method is that the liquid is easy to leak, and the thermal contact resistance is large, which affects the cooling efficiency of the micro-channel [45]. In contrast, the existing 3D printing technology can be formed in one piece with a better sealing effect, which can completely avoid the above defects. Therefore, in this work, according to the optimal structural parameters obtained by MSTV-BTMS optimization design, the optimized MSTV channel is processed by the metal 3D printing method, and its material is set as aluminum alloy $AlSi_{10}Mg$. The internal quality of the flow channel after printing and molding is tested by hydrodynamic tightness to ensure no blockage and leakage in the microchannel. As shown in Figure 15a,b, the microchannel did not leak under the condition of inlet pressure of 0.4 MPa and holding pressure for 30 min, indicating that the sample part confinement met the requirements [46]. In addition, Figure 15c shows the internal channel morphology of the sample.

The experimental system is shown in Figure 16a, which mainly consisted of the liquid supply module, cooling plate, lithium-ion battery charge/discharge cycle module, and temperature and pressure measurement module. The liquid supply module included a peristaltic pump (DIP1500-S183), flow meter (AI-DFT-V01), water tank (ART27), and condenser (PT3600). The lithium-ion battery charge and discharge cycle module included a square lithium-ion battery and load box (DCL8006). The temperature and pressure measuring module included a K-type thermocouple, a temperature-measuring device (TAD-6407), and a draft indicator (SIN-P300-B). The accuracy of each instrument is shown in Table 8. It is not difficult to find that the accuracy range of each instrument was within the acceptable range.

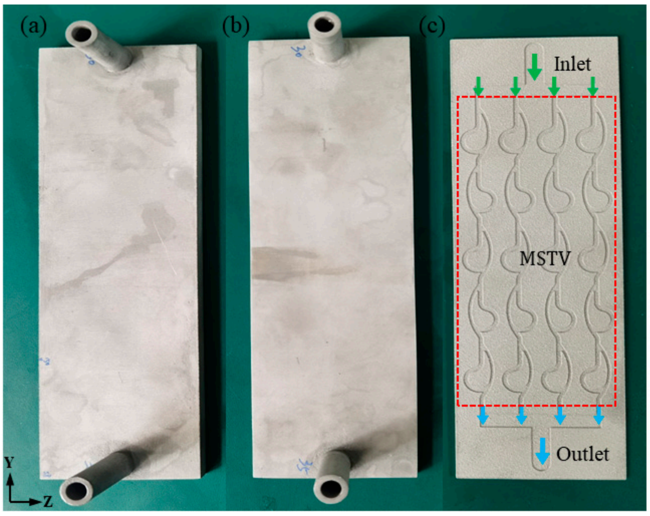

Figure 15. The 3D-printed microchannel sample: (**a**) cold plate—I; (**b**) cold plate—II; (**c**) internal channel of MSTV.

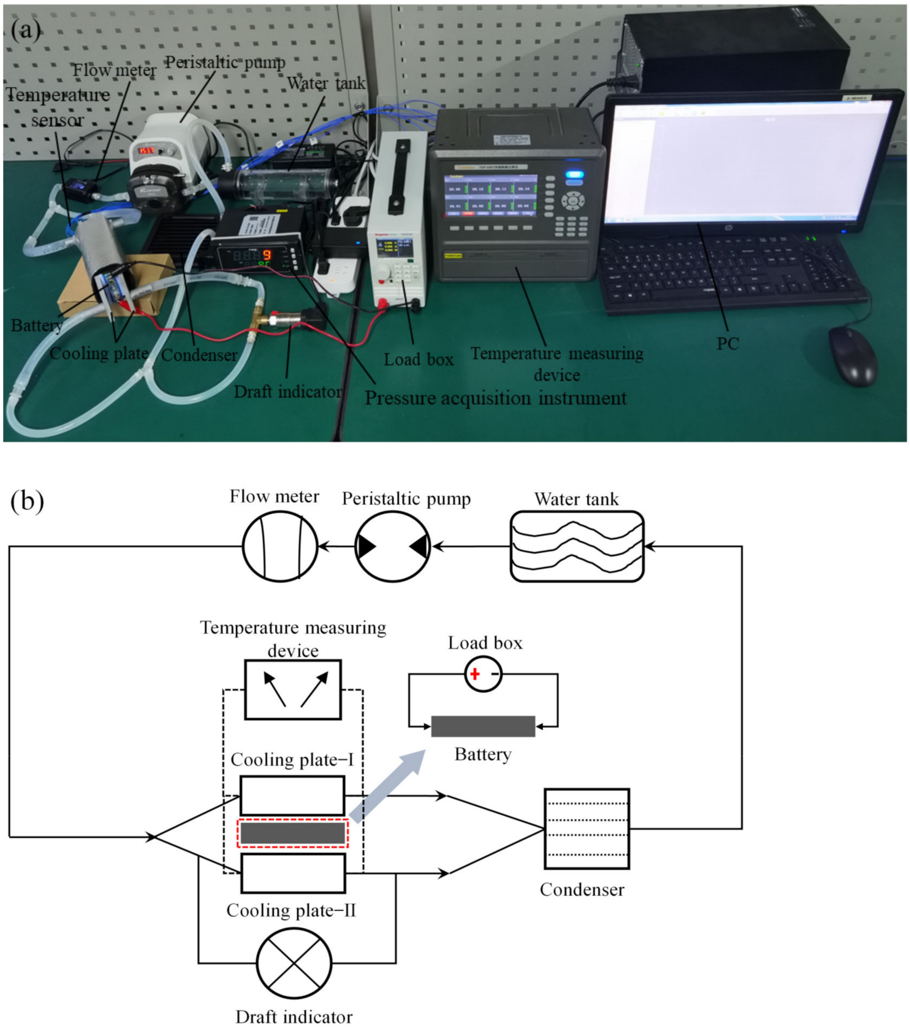

Figure 16. Cold plate experimental platform: (**a**) schematic diagram of coolant flow direction; (**b**) actual experimental platform.

Table 8. Range and accuracy of related instruments in the experiment.

Experimental Instruments	Range	Accuracy
Peristaltic pump (DIP1500-S183)	0∼1500 mL·min^{-1}	±5%
Flow meter (AI-DFT-V01)	−20∼110 °C; 5∼200 mL·min^{-1}	±2.5%
Draft indicator (SIN-P300-B)	−0.1∼60 MPa	±0.1% FS
Load box (DCL8006A)	0∼500 V; 0∼30 A	0.1% + 5 mV, 0.1% + 10 mA
Temperature-measuring device (TAD-6407)	−200∼600 °C	±0.2% FS
Temperature sensor (k-type)	−50∼260 °C	±0.15 °C
Water tank (ART27)	14.4 L; 5∼100 °C	±0.5 °C
Condenser (PT3600)	25∼70 °C	±1 °C

5.2. Performance Analysis of Optimal MSTV-BTMS

5.2.1. Comparison and Error Analysis between the Experimental Validation and Numerical Calculation

On the basis of the above MSTV-BTMS optimization results, during the experiment, the coolant was first set to be water with the initial temperature T_{amb} = 30 °C, and the coolant was filled with the water tank. Following this, the peristaltic pump was adjusted, and we observed the flow meter to show the value of 2.77 L/min (Re = 243), where the coolant flow direction is shown in Figure 16b. Finally, we then started the load box, adjusted it to the lithium-ion battery to measure the working condition (4 C discharge rate), and obtained the temperature data of the battery and the pumping power consumption of the cooling plate.

As can be seen from Figure 17, the optimization results were verified by experiments and had good consistency. Among them, the maximum temperature of the lithium-ion battery optimized by the algorithm was 34.5 °C, and their error was 2.7% compared with the experimental verification results (33.59 °C). The surface standard deviation of the lithium-ion battery and the error of the pressure drop of the plate with the MSTV channel were 10.4% and 3.3%, respectively. Therefore, the CFD method and algorithm optimization design used were very effective for evaluating the performance of MSTV-BTMS. Compared with the ideal operational environment in the simulation, these minor errors resulted from the following differences in the experiment: (1) Due to interference from humans and machines, the ambient temperature of the laboratory was slightly lower than 30 °C. (2) The MSTV channel was formed by 3D printing. Its accuracy was ±0.2 mm, which cannot meet the accuracy requirements of the optimal design. (3) The microchannel surface of the 3D printing also was unable to reach the absolute smoothness requirement in the simulation. (4) In the experiment, the inevitable hydraulic loss in the flow channel resulted in a pressure rise.

In addition, it can be found that the initial MSTV channel geometric parameters were optimized by the algorithm, which significantly improved the cooling performance of the lithium-ion battery and the pump power consumption of the cold plate. As shown in Table 9, the maximum temperature and surface standard deviation of the lithium-ion battery decreased by 7.7% and 40.6%, respectively. The pressure drop required to drive the coolant flow dropped to 23.5%.

Table 9. Performance comparison between the optimal design and initial design.

	T_{max}	T_{σ}	ΔP
Optimal design vs. initial design (%)	7.7	40.6	23.5

5.2.2. Comparison of Thermal Cooling Performance of Typical Liquid Cooling Channels

In this study, the advantages of a cold plate with the MSTV channel and serpentine channel were further compared. Due to the difference of the two channel structures (cooling channel extension routes), they were ensured to have the same coolant volume fraction and the same basic geometric parameters (d, W, and r_x). In addition, according to the length (L_y) and width (L_x) of the MSTV cold plate, it was determined that the number of straight-through channels was seven, the channel width (d) was 2 mm, the ridge width (ε) was 6.285 mm, and the thickness (W) was 0.94 mm, as shown in Figure 18.

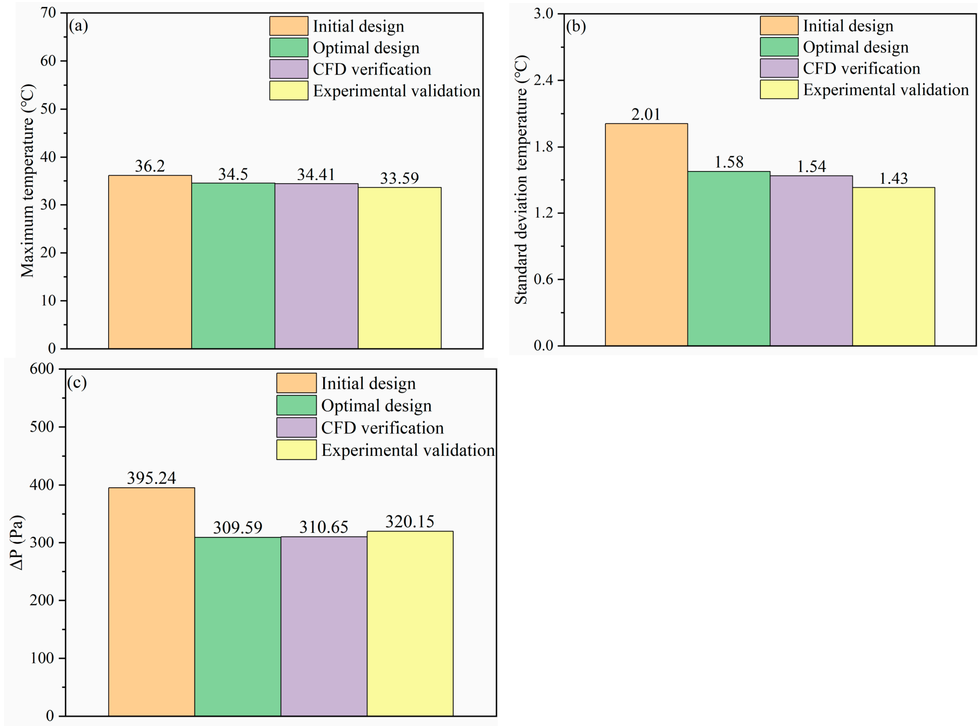

Figure 17. Comparison between the experiments and numerical calculation: (**a**) maximum temperature; (**b**) temperature standard deviation; (**c**) energy cost.

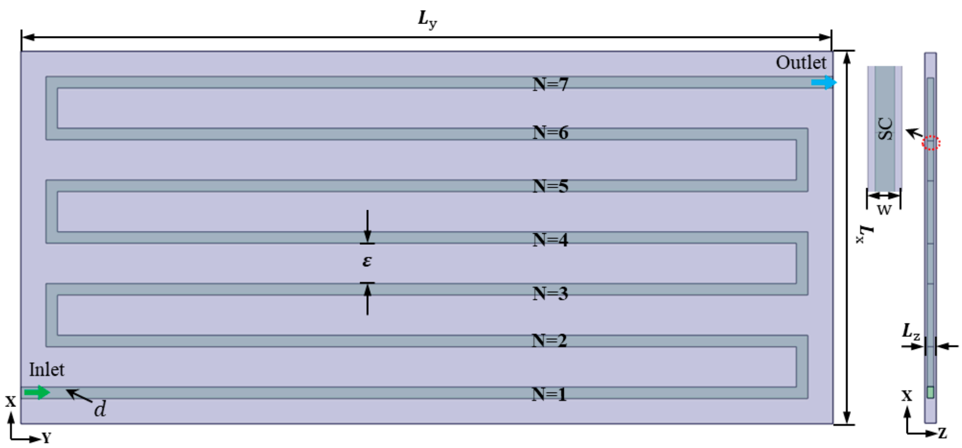

Figure 18. Schematic diagram of the cold plate with the serpentine channel.

Figure 19 shows the temperature profiles of the MSTV channel heat exchanger and the traditional serpentine channel at the same inlet velocity (coolant flow rate was 2.77 L/min). It can be seen from Figure 19a-1,b-1 that there was a great difference in the maximum temperature (the MSTV channel was 31.2 °C; the serpentine channel was 33.3 °C) of the internal channel of the two heat exchangers. In the cold plate of the MSTV channel, the heat transfer between channels at all levels was interrelated, among which the most obvious was the interaction between the zero-stage Tesla valve channel and its adjacent final stage channel, with little overall temperature difference. However, in the cold plate of the serpentine channel, the surface standard deviation of the whole cold plate was large (about 3.1 °C) because the outlet and inlet of the coolant were arranged on the left and right side of the cold plate. In contrast, the surface standard deviation of the cold plate in the MSTV channel was only 1.1 °C, and the small surface standard deviation was only distributed at the coolant outlet.

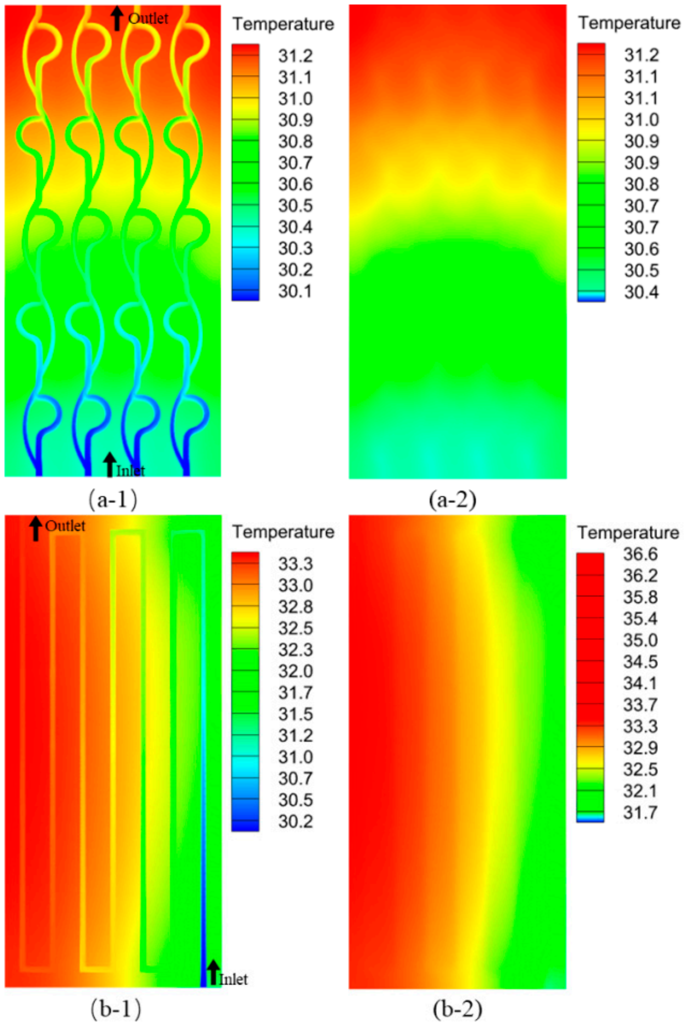

Figure 19. Temperature profiles of two channel structures: (**a-1**) the MSTV channel; (**a-2**) the surface of a lithium-ion battery cold plate with the MSTV channel; (**b-1**) serpentine channel; (**b-2**) the surface of a lithium-ion battery cold plate with the serpentine channel.

To better highlight the cooling performance of the MSTV channel cold plate for lithium-ion batteries, the temperature distribution of the same lithium-ion battery cross-section was compared, as shown in Figure 19a-2,b-2. It can be clearly found that using the cooling plate of the MSTV channel for cooling the lithium-ion battery, its maximum temperature was 31.2 °C. However, the temperature of the lithium battery cooled by the serpentine channel was 36.6 °C, and the difference between the two was 17.3%.

6. Conclusions

In this study, a novel MSTV configuration was proposed and numerically evaluated to mitigate the temperature gradient and pump power consumption issues of the conventional serpentine-channel-based cold plate for the thermal management of a prismatic battery. Moreover, multi-objective optimization was carried out using the NCGA genetic algorithm, and the optimization design of MSTV-BTMS under the condition of high rate (4 C) discharge of lithium-ion batteries was verified in the experiment. The main conclusions can be described as follows:

(1) Sensitivity analysis proved that the MSTV channel had the most significant effect on the temperature distribution uniformity of the lithium-ion battery (90%) and the

energy cost of the MSTV-BTMS (87%). A suitable coolant flow rate can significantly improve the maximum temperature of a lithium-ion battery (77%).

(2) Through a multi-objective optimization design on the valve of the MSTV channel spacing, the thickness, and the coolant flow rate, the maximum temperature and the surface standard deviation of a lithium-ion battery can be decreased by 7.7% and 40.6%, respectively. The pump energy consumption to drive the coolant flow was reduced to 23.5%.

(3) The accuracy of the model was verified by experiments, and the errors of maximum temperature difference and the surface standard deviation of a lithium-ion battery were 2.7% and 10.4%, respectively. Moreover, the energy consumption of the pump undertaken to drive the coolant flow was reduced to 23.5 %. The error was considered within the allowable range.

(4) Compared to the traditional serpentine channel, the optimized MSTV-BTMS had a 17.3% better cooling performance.

(5) The future work in extension of the current study would be to focus on the experimental investigations of a 12 Ah prismatic battery module integrated with the proposed liquid cooling plate. Moreover, tests carried out under real-time driving conditions in electric vehicles, such as normalized profile, can be of great interest. In addition, the effects of varying hydraulic diameter, inner curve radius in each Tesla valve, valve angle, number of valves in the MSTV structure, and corresponding optimization of the cooling plate structure can be considered the scope of future work.

Author Contributions: Conceptualization, Y.F.; Methodology, Y.F.; Software, Y.F. and X.X.; Validation, Z.W.; Investigation, S.P., R.F. and M.F.; Resources, X.X.; Writing—Original Draft, Y.F.; Writing—Review and Editing, Z.W.; Supervision, Z.W.; Project Administration, Z.W.; Funding Acquisition, Z.W. All authors have read and agreed to the published version of the manuscript.

Funding: This research was funded by the National Natural Science Foundation of China (no. 51875419) and the independent innovation project of Longzhong Laboratory in Hubei Province (no. 2022ZZ-14). Moreover, the numerical simulation of many cases was supported by the High-Performance Computing Center of the Wuhan University of Science and Technology.

Data Availability Statement: Not applicable.

Conflicts of Interest: The authors declare no conflict of interest.

Nomenclature

A_{ch}	Cross-sectional area of a channel, (m^2)
C_b	heat capacity, (J·kg^{-1}·K^{-1})
d	channel width, (mm)
D_h	inlet hydraulic diameter, (m)
G	valve distance, (mm)
h_b	convection heat transfer coefficient, (W·m^{-1}·K^{-1})
k	thermal conductivity, (W·m^{-1}·K^{-1})
N	number of stages
p	static pressure of the coolant, (Pa)
P	the perimeter inlet of the MSTV channel, (m^2)
q_{gen}	heat production power of the battery, (W)
q_{abs}	heat absorption power of the battery, (W)
Re	Reynolds number
R_x	x direction machining limit
T	temperature, (°C)
$\overline{T}$	the mean of bottom temperature, (°C)
V	velocity, (m·s^{-1})
W	channel thickness, (mm)
μ_c	coolant volume fraction
x, y, z	coordinates, (mm)

Greek symbols	
ρ	density, (kg·m^{-3})
μ	viscosity, (Pa·s)
σ	standard deviation
ε	channel ridge width, (mm)
∇	gradient
Subscripts	
b	battery
c	coolant
max	maximum
min	minimum
Acronyms	
BTMS	battery thermal management system
CFD	computational fluid dynamics
DOE	design of experiments
EVs	electric vehicles
NCGA	neighborhood cultivation genetic algorithm
MSTV	multi-stage Tesla valve
SC	serpentine channel
TC	thermocouple

Appendix A

Run	Design Variables			Objective Function		
	G	W	Re	T_{max} (°C)	T_σ(°C)	ΔP (Pa)
1	11.7	0.2	150	36.9	1.63	221.00
2	15.56	1.27	300	35.7	1.61	465.49
3	14.3	1.27	300	35.7	1.62	464.82
4	14.3	1.27	225	35.7	1.61	306.39
5	15.56	1.27	225	35.7	1.61	306.81
6	14.3	0.73	300	36.0	1.61	511.55
7	15.56	0.73	300	36.0	1.60	511.54
8	11.7	0.2	300	36.0	1.62	509.89
9	11.7	0.73	300	36.0	1.62	509.65
10	14.3	1.27	150	36.1	1.61	175.96
11	15.56	1.27	150	36.1	1.60	176.12
12	14.3	0.73	225	36.3	1.61	357.39
13	15.56	0.73	225	36.3	1.60	357.20
14	11.7	0.2	225	36.3	1.62	356.23
15	11.7	0.73	225	36.3	1.62	356.21
16	14.3	0.73	150	36.9	1.62	221.62
17	11.7	0.73	150	36.9	1.63	221.06
18	15.56	0.73	150	36.9	1.62	221.37
19	14.3	1.27	75	37.2	1.63	72.29
20	15.56	1.27	75	37.2	1.62	72.31
21	13.05	1.27	300	38.0	1.68	3594.86
22	13.05	0.2	300	38.0	1.68	3595.56
23	14.3	0.2	300	38.0	1.68	3585.91
24	13.05	0.73	300	38.0	1.68	3591.04
25	13.05	1.8	300	38.0	1.68	3597.27
26	15.56	0.2	300	38.0	1.68	3574.68
27	11.7	0.73	75	38.3	1.67	100.49
28	11.7	0.2	75	38.3	1.67	100.44
29	14.3	0.73	75	38.3	1.67	100.62
30	15.56	0.73	75	38.3	1.66	100.48
31	13.05	1.27	225	38.6	1.67	2641.39
32	13.05	0.2	225	38.6	1.67	2641.81
33	14.3	0.2	225	38.6	1.67	2635.37
34	15.56	0.2	225	38.6	1.67	2626.88
35	13.05	1.8	225	38.6	1.67	2642.74
36	13.05	0.73	225	38.6	1.67	2638.49
37	13.05	1.27	150	39.2	1.58	1731.20
38	13.05	0.2	150	39.2	1.58	1731.43
39	14.3	0.2	150	39.2	1.58	1727.55
40	15.56	0.2	150	39.2	1.58	1721.94
41	13.05	1.8	150	39.2	1.59	1732.05
42	13.05	0.73	150	39.2	1.59	1729.29
43	14.3	0.2	75	39.8	1.32	839.72
44	13.05	1.27	75	39.8	1.32	841.36
45	15.56	0.2	75	39.8	1.32	836.91
46	13.05	0.2	75	39.8	1.31	817.82
47	13.05	1.8	75	39.8	1.32	841.87
48	13.05	0.73	75	39.8	1.32	840.54
49	11.7	1.8	300	43.6	1.65	403.58
50	11.7	1.8	225	43.7	1.64	256.90
51	11.7	1.8	150	43.9	1.64	141.71
52	11.7	1.8	75	44.5	1.64	54.94
53	14.3	1.8	300	44.6	1.65	403.88

Run	Design Variables			Objective Function		
	G	W	Re	T_{max} (°C)	T_{σ}(°C)	ΔP (Pa)
54	14.3	1.8	225	44.8	1.64	257.38
55	14.3	1.8	150	45	1.64	142.07
56	14.3	1.8	75	45.5	1.64	55.07
57	15.56	1.8	300	44.9	1.69	403.19
58	15.56	1.8	225	45.0	1.69	257.40
59	15.56	1.8	150	45.4	1.68	142.15
60	15.56	1.8	75	46.3	1.69	55.05
61	11.7	1.27	300	39.2	1.65	403.56
62	11.7	1.27	225	39.4	1.65	257.15
63	11.7	1.27	150	39.6	1.64	141.97
64	11.7	1.27	75	40.4	1.64	55.00

References

1. Zhang, X.; Li, Z.; Luo, L.; Fan, Y.; Du, Z. A review on thermal management of lithium-ion batteries for electric vehicles. *Energy* **2022**, *238*, 121652. [CrossRef]
2. Liu, H.; Wei, Z.; He, W.; Zhao, J. Thermal issues about Li-ion batteries and recent progress in battery thermal management systems: A review. *Energy Convers. Manag.* **2017**, *150*, 304–330. [CrossRef]
3. Mali, V.; Saxena, R.; Kumar, K.; Kalam, A.; Tripathi, B. Review on battery thermal management systems for energy-efficient electric vehicles. *Renew. Sust. Energ. Rev.* **2021**, *151*, 111611. [CrossRef]
4. Putra, N.; Sandi, A.F.; Ariantara, B.; Abdullah, N.; Mahlia, T.M.I. Performance of beeswax phase change material and heat pipe as passive battery cooling system for electric vehicles. *Case Stud. Therm. Eng.* **2020**, *21*, 100655. [CrossRef]
5. Guo, R.; Li, L. Heat dissipation analysis and optimization of lithium-ion batteries with a novel parallel-spiral serpentine channel liquid cold plate. *Int. J. Heat Mass Transf.* **2022**, *189*, 122706. [CrossRef]
6. Huang, Y.; Wei, C.; Fang, Y. Numerical investigation on optimal design of battery cold plate for uneven heat generation conditions in electric vehicles. *Appl. Therm. Eng.* **2022**, *211*, 118476. [CrossRef]
7. Xie, J.; Wang, Y.; He, S.; Zhang, G.; Liu, X.; Yang, X. A simple cooling structure with precisely-tailored liquid cold plate for thermal management of large battery module. *Appl. Therm. Eng.* **2022**, *212*, 118575. [CrossRef]
8. Li, J.; Zuo, W.; Jiaqiang, E.; Zhang, Y.; Li, Q.; Sun, K.; Zhou, K.; Zhang, G. Multi-objective optimization of mini U-channel cold plate with SiO_2 nanofluid by RSM and NSGA-II. *Energy* **2022**, *242*, 123039. [CrossRef]
9. Zhai, Y.; Xia, G.; Li, Z.; Wang, H. A novel flow arrangement of staggered flow in double-layered microchannel heat sinks for microelectronic cooling. *Int. Commun. Heat Mass Transf.* **2016**, *79*, 98–104. [CrossRef]
10. Larrañaga-Ezeiza, M.; Vertiz, G.; Arroiabe, P.F.; Martinez-Agirre, M.; Berasategi, J. A novel direct liquid cooling strategy for electric vehicles focused on pouch type battery cells. *Appl. Therm. Eng.* **2022**, *216*, 118869. [CrossRef]
11. Murray, C.D. The physiological principle of minimum work: II. Oxygen exchange in capillaries. *Proc. Natl. Acad. Sci. USA* **1926**, *12*, 299–304. [CrossRef] [PubMed]
12. Bejan, A.; Lorente, S. Constructal theory of generation of configuration in nature and engineering. *J. Appl. Phys.* **2006**, *100*, 5. [CrossRef]
13. He, P.; Lu, H.; Fan, Y.; Ruan, H.; Wang, C.; Zhu, Y. Numerical investigation on a lithium-ion battery thermal management system utilizing a double-layered I-shaped channel liquid cold plate exchanger. *Int. J. Therm. Sci.* **2023**, *187*, 108200. [CrossRef]
14. Qi, W.; Huang, W.; Niu, J.; Chen, F.; Chen, B.; Chen, Y. Thermal management of power battery based on flexible Swiss roll type liquid cooling micro-channel. *Appl. Therm. Eng.* **2023**, *219*, 119491. [CrossRef]
15. Wu, X.; Mo, C.; Li, X.; Li, C.; Lin, R.; Zeng, Y.; Cao, J.; Liu, X. Experiment investigation on optimization of cylinder battery thermal management with microchannel flat tubes coupled with composite silica gel. *J. Power Sources* **2022**, *56*, 105871. [CrossRef]
16. Gamboa, A.R.; Morris, C.J.; Forster, F.K. Improvements in fixed-valve micropump performance through shape optimization of valves. *J. Fluids Eng.* **2005**, *127*, 339–346. [CrossRef]
17. Tuckerman, D.B.; Pease, R.F.W. High-performance heat sinking for VLSI. *IEEE Electron Device Lett.* **1981**, *2*, 126–129. [CrossRef]
18. Monika, K.; Chakraborty, C.; Roy, S.; Sujith, R.; Datta, S.P. A numerical analysis on multi-stage Tesla valve based cold plate for cooling of pouch type Li-ion batteries. *Int. J. Heat Mass Transf.* **2021**, *177*, 121560. [CrossRef]
19. Rui, Z.; Zhao, F.; Sun, H.; Sun, L.; Peng, H. Experimental research on flow boiling thermal-hydraulic characteristics in novel microchannels. *Exp. Therm. Fluid Sci.* **2023**, *140*, 110755. [CrossRef]
20. Sun, L.; Li, J.; Xu, H.; Ma, J.; Peng, H. Numerical study on heat transfer and flow characteristics of novel microchannel heat sinks. *Int. J. Therm. Sci.* **2022**, *176*, 107535. [CrossRef]
21. Bao, Y.; Wang, H. Numerical study on flow and heat transfer characteristics of a novel Tesla valve with improved evaluation method. *Int. J. Heat Mass Transf.* **2022**, *187*, 122540. [CrossRef]

22. Li, X.; Zhang, X.; Li, W.; Wang, Z.; Zhang, X.; Zhao, Y. The 3D Tesla Valve Manifold Two-Phase Cold plate for the SiC Power Device Module. In Proceedings of the 2022 21st IEEE Intersociety Conference on Thermal and Thermomechanical Phenomena in Electronic Systems (iTherm), San Diego, CA, USA, 31 May–1 June 2022; pp. 1–8. [CrossRef]
23. Fan, Y.; Wang, Z.; Xiong, X.; Zhu, J.; Gao, Q.; Wang, H.; Wu, H. Novel concept design of low energy hybrid battery thermal management system using PCM and multistage Tesla valve liquid cooling. *Appl. Therm. Eng.* **2023**, *220*, 119680. [CrossRef]
24. Porwal, P.R.; Thompson, S.M.; Walters, D.K.; Jamal, T. Heat transfer and fluid flow characteristics in multistaged Tesla valves. *Numer. Heat Transf. Part A Appl.* **2018**, *73*, 347–365. [CrossRef]
25. De Vries, S.F.; Florea, D.; Homburg, F.G.A.; Frijns, A.J.H. Design and operation of a Tesla-type valve for pulsating heat pipes. *Int. J. Heat Mass Transf.* **2017**, *105*, 1–11. [CrossRef]
26. Liang, L.; Zhao, Y.; Diao, Y.; Ren, R.; Zhang, L.; Wang, G. Optimum cooling surface for prismatic lithium-ion battery with metal shell based on anisotropic thermal conductivity and dimensions. *J. Power Sources* **2021**, *506*, 230182. [CrossRef]
27. Drake, S.J.; Wetz, D.A.; Ostanek, J.K.; Miller, S.P.; Heinzel, J.M.; Jain, A. Measurement of anisotropic thermophysical properties of cylindrical Li-ion cells. *J. Power Sources* **2014**, *252*, 298–304. [CrossRef]
28. Chen, S.; Zhang, G.; Zhu, J.; Feng, X.; Wei, X.; Ouyang, M.; Dai, H. Multi-objective optimization design and experimental investigation for a parallel liquid cooling-based lithium-ion battery module under fast charging. *Appl. Therm. Eng.* **2022**, *211*, 118503. [CrossRef]
29. Sheng, L.; Su, L.; Zhang, H. Experimental determination on thermal parameters of prismatic lithium-ion battery cells. *Int. J. Heat Mass Transf.* **2019**, *139*, 231–239. [CrossRef]
30. Bernardi, D.; Pawlikowski, E.; Newman, J. A general energy balance for battery systems. *J. Electrochem. Soc.* **1985**, *132*, 5. [CrossRef]
31. Peng, X.; Ma, C.; Garg, A.; Bao, N.; Liao, X. Thermal performance investigation of an air-cooled lithium-ion battery pack considering the inconsistency of battery cells. *Appl. Therm. Eng.* **2019**, *153*, 596–603. [CrossRef]
32. Panchal, S. Experimental Investigation and Modeling of Lithium-Ion Battery Cells and Packs for Electric Vehicles. Ph.D. Thesis, Ontario Tech University, Oshawa, ON, Canada, 2016. Available online: https://hdl.handle.net/10155/747 (accessed on 1 January 2016).
33. Fan, Y.; Wang, Z.; Fu, T.; Wu, H. Numerical investigation on lithium-ion battery thermal management utilizing a novel tree-like channel liquid cold plate exchanger. *Int. J. Heat Mass Transf.* **2022**, *183*, 122143. [CrossRef]
34. Bahiraei, F.; Fartaj, A.; Nazri, G.A. Electrochemical-thermal modeling to evaluate active thermal management of a lithium-ion battery module. *Electrochim. Acta* **2017**, *254*, 59–71. [CrossRef]
35. Huang, H.; Wang, H.; Gu, J.; Wu, Y. High-dimensional model representation-based global sensitivity analysis and the design of a novel thermal management system for lithium-ion batteries. *Energy Convers. Manag.* **2019**, *190*, 54–72. [CrossRef]
36. Zhao, R.; Gu, J.; Liu, J. Optimization of a phase change material based internal cooling system for cylindrical Li-ion battery pack and a hybrid cooling design. *Energy* **2017**, *135*, 811–822. [CrossRef]
37. Ghaedamini, H.; Salimpour, M.R.; Campo, A. Constructal design of reverting microchannels for convective cooling of a circular disc. *Int. J. Therm. Sci.* **2011**, *50*, 1051–1061. [CrossRef]
38. Hung, T.C.; Yan, W.M.; Wang, X.D.; Huang, Y.X. Optimal design of geometric parameters of double-layered microchannel heat sinks. *Int. J. Heat Mass Transf.* **2012**, *55*, 3262–3272. [CrossRef]
39. Kechagias, J.D.; Aslani, K.E.; Fountas, N.A.; Vaxevanidis, N.M.; Manolakos, D.E. A comparative investigation of Taguchi and full factorial design for machinability prediction in turning of a titanium alloy. *Measuremen* **2020**, *151*, 107213. [CrossRef]
40. Kleijnen, J.P. Kriging metamodeling in simulation: A review. *Eur. J. Oper. Res.* **2009**, *192*, 707–716. [CrossRef]
41. Ulaganathan, S.; Couckuyt, I.; Deschrijver, D.; Laermans, E.; Dhaene, T. A Matlab toolbox for Kriging metamodelling. *Procedia Comput. Sci.* **2015**, *51*, 2708–2713. [CrossRef]
42. Watanabe, S.; Hiroyasu, T.; Miki, M. Neighborhood cultivation genetic algorithm for multi-objective optimization problems. In Proceedings of the 4th Asia-Pacific Conference on Simulated Evolution and Learning (SEAL-2002), Singapore, 18–22 November 2002; pp. 198–202. [CrossRef]
43. Bagherzadeh, S.A.; D'Orazio, A.; Karimipour, A.; Goodarzi, M.; Bach, Q.V. A novel sensitivity analysis model of EANN for F-MWCNTs–Fe_3O_4/EG nanofluid thermal conductivity: Outputs predicted analytically instead of numerically to more accuracy and less costs. *Phys. A* **2019**, *521*, 406–415. [CrossRef]
44. Alrashed, A.A.; Gharibdousti, M.S.; Goodarzi, M.; de Oliveira, L.R.; Safaei, M.R.; Bandarra Filho, E.P. Effects on thermophysical properties of carbon based nanofluids: Experimental data, modelling using regression, ANFIS and ANN. *Int. J. Heat Mass Transf.* **2018**, *125*, 920–932. [CrossRef]
45. Kandlikar, S.G.; Grande, W.J. Evolution of microchannel flow passages–thermohydraulic performance and fabrication technology. *Heat Transf. Eng.* **2003**, *24*, 3–17. [CrossRef]
46. Lee, J.; Darges, S.J.; Mudawar, I. Experimental investigation and analysis of parametric trends of instability in two-phase micro-channel heat sinks. *Int. J. Heat Mass Transf.* **2021**, *170*, 120980. [CrossRef]